Integrative Modelling of Signalling Network Dynamics Identifies Cell Type-selective Therapeutic Strategies for FGFR4-driven Cancers

Sung-Young Shin[1,2,*], Nicole J Chew[1,2,*], Milad Ghomlaghi[1,2], Anderly C Chüeh[1,2], Lan K. Nguyen[1,2,#] and Roger J Daly[1,2,#]

[1]Cancer Program, Biomedicine Discovery Institute, Monash University, Melbourne, VIC 3800, Australia.
[2] Department of Biochemistry and Molecular Biology, Monash University, Melbourne, VIC 3800, Australia.

* These authors contributed equally to the work
[#] Correspondence: roger.daly@monash.edu; lan.k.nguyen@monash.edu

Abstract

Oncogenic FGFR4 signalling represents a potential therapeutic target in many cancer types, including triple negative breast cancer (TNBC) and hepatocellular carcinoma (HCC). However, resistance to single-agent therapy directed at FGFR4 remains a major challenge, prompting the need to identify more effective combinatorial therapeutic strategies. Here, we integrated computational network modelling and experimental validation to characterise dynamic reprogramming of the FGFR4 signalling network in TNBC following FGFR4 kinase inhibition. We found that AKT, which signals downstream of FGFR4, displayed a rapid and potent reactivation following FGFR4 targeting. Through model-based simulation and systematic prediction of the effect of co-targeting specific network nodes, we predicted, and validated experimentally, strong synergism of co-targeting FGFR4 and particular ErbB kinases or AKT, but not the upstream kinase PI3K. Further, incorporation of protein expression data from hundreds of cancer cell types enabled us to adapt our model to other diverse cellular contexts, leading to the prediction that while AKT rebound occurs frequently, it is not a general phenomenon. Instead, ERK is reactivated in a subset of cell types, including the FGFR4-driven HCC cell line Hep3B. This was subsequently corroborated, and moreover, co-targeting FGFR4 and MEK in Hep3B cells markedly enhanced inhibition of cell proliferation. Overall, these findings provide novel insights into the dynamics of drug-induced network remodelling in cancer cells, highlight the impact of protein expression heterogeneity on network response to targeted therapy and identify candidate cell type-selective combination treatments for FGFR4-driven cancer.

Keywords
Combination therapy, network rewiring, signal transduction, mechanistic modelling, in silico simulation.

Introduction

Aberrant signalling by specific members of the FGFR family, comprising FGFR1-4, occurs in a variety of human cancers, and can reflect FGFR gene mutation, fusion, amplification and/or overexpression, and also altered ligand expression (1). This has led to the development of selective small molecule drugs targeting these receptors, including Erdafitinib (an inhibitor of FGFR1-4), which was recently FDA-approved for patients with metastatic urothelial carcinoma exhibiting FGFR2/3 gene alterations and resistance to chemotherapy (2). While initial interest focused on FGFR1-3, oncogenic roles for FGFR4 in a variety of cancers have now become evident (3). In breast cancer, enhanced FGFR4 expression and mutation is associated with metastatic progression, particularly in the lobular subtype (4), and high FGFR4 expression positively correlates with endocrine resistance (4, 5). FGFR4 also drives phenotypic switching of luminal A breast cancers to a HER2-enriched gene expression phenotype (6), and is overexpressed in approximately one third of triple negative breast cancers (TNBCs) (7). A second cancer where FGFR4 is strongly implicated is hepatocellular carcinoma (HCC). Here, FGFR4 is activated as a consequence of overexpression of its ligand, FGF19, which is a 'driver' oncogene on the chromosome 11q13.3 amplicon (8). Reflecting this mechanism, FGF19 represents a predictive biomarker for response to anti-FGFR4 therapy across HCC cell lines and patient-derived xenografts (9). The accumulated evidence supporting oncogenic roles for FGFR4 has led to the development of BLU9931, BLU-554 (fisogatinib) and H3B-6527, small molecule drugs that selectively target and irreversibly bind this receptor. These drugs all exhibit promising pre-clinical activity in FGF19-driven HCC (9-11) and both fisogatinib and H3B-6527 are currently under evaluation in clinical trials for HCC patients with advanced HCC (NCT04194801 and NCT02834780).

While targeted therapies directed towards specific oncogenic protein kinases have greatly improved clinical management of particular cancers (12), intrinsic and acquired drug resistance remain a major problem. Well-established mechanisms that contribute to these resistance phenotypes include mutation of the target or downstream signalling proteins such as Ras, or the presence of by-pass signalling pathways (13). However, an additional mechanism that can limit the efficacy of targeted therapy is dynamic, adaptive rewiring of the cellular signalling network in response to treatment (1). For example, use of mTOR inhibitors can lead to enhanced PI3K/AKT signalling due to relief of negative feedback regulation of IRS-1 by S6K1, which lies downstream of mTORC1 (14). In addition, treatment with AKT or MEK inhibitors can lead to increased expression and/or activation of a suite of receptor tyrosine kinases (RTKs) that dampens the cellular response to the drug (15, 16). Importantly, characterization of network adaptation in response to drug treatment can inform the rational design of combination therapies that exhibit improved efficacy. For example, since kinome remodelling in response to AKT inhibition involves enhanced expression and activation of ErbB3, co-targeting of AKT and ErbB kinases achieves greater efficacy than either monotherapy (15).

Despite these advances, the complexity of kinase signalling networks presents a major roadblock to understanding mechanisms of adaptive resistance to targeted therapy (1). This complexity reflects the presence of features such as pathway crosstalk and both positive and negative feedback loops, and results in non-intuitive behaviour that makes logical prediction of signalling and biological outputs challenging. A powerful approach to address this issue is to integrate mathematical network modelling with experimental analysis in order to generate and validate predictive models. This can provide fundamental insights into the wiring of signalling networks and how this generates specific signalling behaviours and biological outputs. For example, application of this approach revealed the network basis for discriminating distinct ERK activity dynamics (17) and identified the incoherent feed-forward loop as a design principle underpinning network regulation of cell fate switching (18). In addition, it can be exploited to identify novel therapeutic strategies, as exemplified by accurate prediction of synergistic drug combinations stemming from establishment of a quantitative mechanistic model of the EGFR-PYK2-MET signalling network in triple negative breast cancer (19).

In this study, we developed a detailed mechanistic model of the FGFR4 signalling network and applied an integrative approach combining computational modelling and experimental studies to interrogate the dynamic rewiring of this network to anti-FGFR4 inhibition in cancer cells and identify combinatorial approaches that prevent or circumvent drug resistance. In addition, our work established new general quantitative metrics that characterise drug-induced rebound behaviours, and by generating cell type specific models through incorporation of protein expression data from hundreds of different cancer cell types, we demonstrate a remarkable diversity and heterogeneity in the signalling responses to FGFR4 inhibition across various and distinct cellular contexts. Overall, our work establishes an integrative framework for the network-level analysis of drug-induced signalling adaptation that can be applied not only to FGFR4 inhibition but also other kinase-directed targeted therapies.

Materials and Methods

Cell lines, cell culture and reagents

The TNBC cell line, MDA-MB-453 and HCC cell line, Hep3B were purchased from ATCC. MDA-MB-453 was cultured in RPMI-1640 (Gibco) supplemented with 10% (v/v) FBS (Moregate), 10 µg/mL Actrapid penfill insulin (Clifford Hallam Healthcare) and 20 mM HEPES (Gibco). Hep3B was cultured in EMEM (USbio) supplemented with 10% (v/v) FBS and 1 mM sodium pyruvate (Gibco). To passage cells, cells were washed once with 1x PBS, then detached from plates with 0.05% (w/v) trypsin/EDTA (Gibco) at 37°C in a 5% CO2 atmosphere. Trypsin was then inhibited with complete media.

For harvesting, cells at 80% confluency were washed twice with ice cold 1x PBS then lysed with RIPA buffer (0.5% (w/v) sodium deoxycholate, 150 mM NaCl, 1% (v/v) NP40, 50 mM Tris-HCl pH 8.0, 0.1% (w/v) SDS, 10% (v/v) glycerol, 5 mM EDTA and 20 mM NaF), supplemented with

10 μg/mL aprotinin, 1 mM PMSF, 10 μg/mL leupeptin, 1 mM sodium orthovanadate, 2.5 mM sodium pyrophosphate and 2.5 mM β-glycerophosphate prior to use. Lysed cells were collected and clarified by centrifugation at 21130 x *g* at 4°C for 10 min, then the protein concentration was determined using a Pierce BCA protein assay kit (Thermoscientific) according to the manufacturer's protocol.

Inhibitors and treatment

The following inhibitors were purchased from Selleckchem: FGFR4 inhibitor BLU9931 and H3B-6527, ErbB family inhibitor Lapatinib, PI3Kα inhibitor BYL719, pan-PI3K inhibitor BKM120, AKT inhibitor MK2206 and MEK inhibitor Trametinib. All inhibitors were reconstituted in DMSO.

For inhibitor treatment, cells were seeded into culture plates with an 80% end point confluence for all cell lines. After 24 h, cells were treated for the indicated times with the specific inhibitor or DMSO as vehicle control.

Generation of FGFR4 inhibitor resistant cells

MDA-MB-453 cells were seeded into 10 cm plates at a density of 500 cells. After 48 h, cells were treated with DMSO (as vehicle control) or FGFR4 inhibitor BLU9931 for at least 3 months. Culture medium was replaced twice a week. When cells formed colonies visible to the naked eye, small pieces of sterile filter paper soaked in trypsin were used to detach cells which were collected for further maintenance in media containing DMSO or FGFR4 inhibitor. These cells were termed long-term BLU9931 MDA-MB-453 cells in this study.

Immunoblotting

Protein lysates (25-40 μg) were prepared in 5x sample loading buffer (9% (v/v) glycerol, 0.03 M Tris/HCl pH 6.8, 2% (w/v) SDS, 0.05% (v/v) β-mercaptoethanol and 0.002% (w/v) bromophenol blue) and boiled for 10 min at 96°C. Western blot analysis was performed using SDS-PAGE on 4% (v/v) stacking gels and 8% (v/v) separating gels. Subsequently, resolved proteins were wet transferred onto PVDF membrane for 1 h, then blocked in 5% (w/v) BSA-TBS (50 mM Tris pH 7.5, 150 mM NaCl) blocking buffer for 1 h at RT, followed by incubation in primary antibody diluted in 5% (w/v) BSA/TBS with rolling overnight at 4°C. Following primary incubation, membranes were washed thrice with TBS-T (50 mM Tris pH 7.5, 150 mM NaCl, 0.1% (v/v) Tween 20) for 10 min, then probed with secondary antibody for 1 h at RT. Membranes were washed thrice again with TBS-T for 10 min before signal detection by ECL (Perkin Elmer) or Luminata Forte Western HRP substrate (Millipore) and images acquired with the ChemiDoc Touch Imaging system (Bio-Rad). Densitometry analysis was performed on the detected bands using ImageLab, version 5.2.1 (Bio-Rad). β-actin or α-tubulin were used as the loading controls. The intensity of each band was normalised against the intensity of their corresponding loading control. Bands corresponding to phospho-proteins were further normalised to the bands of corresponding total protein levels.

The following antibodies were purchased from Cell Signaling Technology: pan-phosFGFR (Y653/654) (3471), AKT (4685), ERK (4695), pAKT (S473) (4058), pERK (T202, Y204) (4370), pFRS2 (Y436) (3861), ALK (3333), pALK (Y1096) (4143), pALK (Y1282/1283) (9687), pALK (Y1078) (4144), ErbB2 (2165), pErbB2 (Y1248) (2247), ErbB3 (4754), pErbB3 (Y1328) (8017), IGF-1R (9750) and GSK (5676). The following antibodies were purchased from Santa Cruz Biotechnology: FGFR4 (sc-136988) and β-actin (sc-69879). The α-tubulin (T5168) and FRS2 (05-502) antibodies were purchased from Sigma-Aldrich. The pIRS-1 (Y612) (44-816G) and pIGF-1R (Y1162/1163) (44-804G) were purchased from Biosource. An IRS-1 (6248) antibody was purchased from Upstate and a pGSK (Y216/279) (ab4797-50) was purchased from Abcam.

Cell viability assays

Cell viability determined by direct cell counting was performed by seeding cells into 6 well plates and culturing for 7 days. Cells were washed with 1x PBS then trypsinised at 37°C in a 5% CO2 atmosphere until detachment. Trypsinised cells were then resuspended thoroughly in complete media to inhibit trypsin. Cells were stained with Trypan blue (EVS-1000, NanoTek), then transferred to an EVE cell counting slide (EVS-1000, NanoTek) and counted with the EVE automatic cell counter (EVE-MC-DEMO, NanoTek) according to the manufacturer's protocol.
For MTS proliferation assays, 3000 cells were seeded into 96 well plates and cultured for the indicated days. Cell viability was determined using the CellTiter 96 Aqueous One Solution Cell Proliferation Assay (Promega) according to the manufacturer's protocol. 20 µL of reagent was added into the wells and incubated at 37°C in a 5% CO2 atmosphere for 45 mins. Absorbance was determined using the PHERAstar microplate reader (BMG LABTECH).

RNA isolation, RT-PCR and Sanger sequencing

Total RNA was isolated from parental MDA-MB-453 and long-term BLU9931 MDA-MB-453 cells using a RNeasy mini kit (Qiagen) following the manufacturer's protocol. RNA was quantified using a Nanodrop ND-1000 (NanoDrop Technologies). RNAs were reverse transcribed using a high-capacity cDNA reverse transcription kit (Thermoscientific). Subsequently, cDNA was amplified by PCR to identify gatekeeper mutations in the FGFR4 kinase domain using forward (F) primers and reverse (R) primers (Table S4). The PCR products were resolved by gel electrophoresis, and the bands at the predicted product size were excised and purified with a gel and PCR clean-up system (Promega). Sanger sequencing was completed by the Micromon facility at Monash University. Reactions were repeated on three biological replicates.

Statistical analysis

Quantification of western blots by densitometry was performed using ImageLab version 5.2.1 (Bio-Rad) and statistical t-tests were performed using GraphPad Prism 8 and Microsoft-Excel.

Computational modelling

The FGFR4-centered model was formulated using ordinary differential equations (ODEs). The rate equations and full set of ODEs are given in Supplementary Tables S1-2. The model construction and calibration processes were implemented in MATLAB (The MathWorks. Inc. 2019a) and the IQM toolbox (http://www.intiquan.com/intiquan-tools/) was used to compile the IQM file for a MEX file which makes the simulation faster. To facilitate model exchange, an exchangeable Systems Biology Markup Language (SBML) file of the model is provided as Supplementary File 1. The code for the modelling has been deposited to Github and can be accessed at https://github.com/NguyenLab-IntegratedNetworkModeling/FGFR4_model.

Model calibration

The adequacy and specificity of a mathematical model is generally justified by its ability to recapitulate experimental data. This is achieved through model calibration (also referred to as model training or fitting) that involves estimation of the unmeasured model parameters so that simulations using these parameter values (called best-fitted parameter sets) could recapitulate the training data. Here, parameter estimation was done by minimizing an objective function J that quantifies the discrepancies between model simulations and the corresponding experimental measurements. A genetic algorithm was used to optimize the objective function (20-22), utilising the Global Optimization Toolbox and the function *ga* in MATLAB. Model calibration was carried out on a virtual machine consisting of 32 Intel Xeon 2.10 GHz processors running in parallel. A more detailed description of the model calibration process is given in Supplementary Text S1. As a result, we obtained 5 best-fitted parameter sets that were collectively used for model simulations; these are given in Supplementary Table S3.

Model-based computation of drug synergy

Using our network model, we evaluated *in silico* the efficacy and possible synergism of 20 possible combinatorial strategies co-targeting FGFR4 and each of 20 network components. Drug synergy was computed based on the coefficient of drug interaction (CDI) metric (23, 24): CDI=$E_{12}/(E_1 \times E_2)$, where E_{12} is a normalized biological response (e.g., cell viability) by the combined treatment of drug 1 and 2, and E_1 and E_2 are the response by the single drug treatment, respectively. CDI <1, = 1 or >1 indicates that the drugs are synergistic, additive or antagonistic, respectively.

To comparatively assess the effect of the single-drug and combination treatments, we introduced a theoretical cell viability (ICV) function, defined as the aggregate of the activated levels of the major pro-growth signalling nodes in the model: $\mathrm{ICV} = [\mathrm{pIGFR}] + [\mathrm{pFGFR4}] + [\mathrm{pERBB}] + [\mathrm{pAKT}] + [\mathrm{aRas}] + [\mathrm{pERK}]$. For each treatment, the corresponding ICV value could be computed using the model. Computationally, a treatment that results in a lower ICV value is assumed to be more effective in suppressing cell viability.

RESULTS

FGFR4 inhibition rewires signalling networks in MDA-MB-453 cells leading to upregulation of AKT activity

To determine the effects of the selective and irreversible FGFR4 inhibitor BLU9931 on FGFR4 downstream signalling and cell proliferation in TNBC, the MDA-MB-453 cell line that exhibits an activating mutation in FGFR4 (25) was utilised. The MDA-MB-468 cell line with no detected FGFRs was used as a negative control (26). MDA-MB-453 cells were treated with different concentrations of BLU9931 for 1 h. Total FGFR4 expression was not affected by BLU9931, but the treatment decreased pFGFR at concentrations of 3nM and higher (Fig. 1A), and this effect was paralleled by a significant decrease in downstream signalling proteins pFRS2, pERK and pAKT (Fig. 1A, B). BLU9931 also significantly decreased cell proliferation of MDA-MB-453 cells at 10nM from day 3 onwards but did not affect MDA-MB-468 cells (Fig. 1C).

To understand how FGFR4 inhibition temporally influences downstream signalling, MDA-MB-453 cells were treated with 10nM of BLU9931 for 1, 4, 8 and 24 h (Fig. 1D). The levels of pFRS2 and pERK were initially decreased, followed by some signal recovery at 24 h (Fig. 1D). However, pAKT levels decreased after 1 h of drug treatment but the signal recovered at 4 h and then increased at 8 h and 24 h relative to the vehicle control (Fig. 1D). This suggests that the FGFR4 signalling network is being dynamically rewired following the inhibitor treatment. To identify if the 'bounce-back' of pAKT is independent of the inhibitor used, MDA-MB-453 cells were treated with another FGFR4 inhibitor, H3B-6527 and this resulted in the same pAKT 'bounce-back' effect at the same time points (Fig. S1A). This suggests a general rewiring phenomenon following FGFR4 inhibition in MDA-MB-453 cells.

A computational mechanistic model of the FGFR4-centred signalling network

The unexpected and marked rebound of pAKT in MDA-MB-453 cells after BLU9931 and H3B-6527 treatment suggests pathway rewiring to compensate the FGFR4 inhibition. Given the complexity of the signalling network surrounding FGFR4, we developed a detailed computational model to achieve a systems-level understanding of the potential compensatory mechanisms in this system. Our model included the major effectors and pro-growth signalling pathways downstream of FGFR4, such as the FRS2, PI3K/AKT/mTOR and Ras/RAF/MEK/ERK signalling pathways. A simplified model scheme is displayed in Fig 2A and the model's detailed reaction map is provided in Fig S2. Since these pathways are also converged upon by other RTKs, the model also incorporated the RTKs of the IGFR/IR and ErbB receptor families. As feedback loops and crosstalk are critical in shaping signalling drug response (30-32), the model (hereafter the 'FGFR4 model') accounted for previously described feedback and crosstalk mechanisms within the integrated FGFR4 network (Fig 2A). The new model was formulated using ordinary differential equations (ODEs) and implemented in MATLAB that mathematically represents the network

interactions based on established kinetic laws (see Materials and Methods and Table S1-2 for detailed model descriptions).

To provide our model with context specificity and predictive capability, we calibrated (trained) it against experimental data using a combination of drug-treated time-course and dose-response signalling data from the MDA-MB-453 cells, as measured by Western blot in Fig. 1A-B,D, and S1B. Model training involved the estimation of unknown model parameters using a genetic algorithm (GA)-based optimisation procedure so that model simulations recapitulated the experimental data (see Materials and Methods). As a result, we obtained five best-fitted parameter sets that were collectively used for further analysis in order to avoid possible biases associated with any single sets (best-fitted parameter values are given in Table S3). Model simulations using the best-fitted sets demonstrated good concordance with the quantified experimental data (Fig. 2B), suggesting the calibrated model could qualitatively and quantitatively reproduce the data.

Co-targeting of FGFR4 and AKT, but not PI3K, eliminates pAKT rebound and suppresses MDA-MB-453 cell proliferation

To determine if the rebound in AKT signals upon treatment with FGFR inhibitors is dependent on the drug dosage, we simulated the temporal response of pAKT to increasing doses of BLU9931 using the calibrated model. Interestingly, the model predicted that at a higher dose (10nM), BLU9931 induced an even stronger rebound in pAKT compared to the lower dose (3nM), that was more pronounced at the later time points (Fig. 3A). Given PI3K is a direct upstream kinase of AKT signalling, we asked if co-targeting FGFR4 with PI3K may eliminate the pAKT rebound. *In silico* model simulations showed that while the combined FGFR and PI3K inhibition (PI3Ki) significantly suppressed pAKT levels at both the early and late time points, the combinatorial treatments did not completely abolish the rebound pattern of pAKT (Fig. 3B,C), which recovered to almost pre-treated levels with the high dose of BLU9931 + PI3Ki (Fig. 3D).

To experimentally validate these model predictions, we treated MDA-MB-453 cells with the PI3K-α inhibitor BYL719 and pan-PI3K inhibitor BKM120 for 1 h at varying concentrations (Fig. S3A,B). These results allowed selection of specific concentrations of each inhibitor to use in combination with BLU9931. Then, MDA-MB-453 cells were treated with BLU9931, BYL719 or BKM120 alone or combinations of BLU9931 with either PI3K inhibitor for 1 and 24 h (Fig. 3E). The highest dose of BLU9931, BYL719 and BKM120 decreased pAKT at 1 h, as did all the combination treatments (Fig. 3E,F). Consistent with model prediction, the higher dose of BLU9931 triggered a stronger rebound of pAKT at 24 h, particularly in the presence of BYL719 (Fig 3E,F). Furthermore, while the BLU9931+BYL719 combination treatments better suppressed the pAKT signal recovery relatively to BLU9931 alone, the combined treatments did not completely eliminate the rebound, as predicted by our model (Fig.3F). This failure to eliminate rebound was similarly observed for the BLU9931+ BKM120 combination (Fig. S4). Next, to determine whether pAKT signal dynamics predict the cellular growth response, we measured cell

314 proliferation in response to the single and combination treatments of BLU9931 and BYL719 or
315 BKM120. Administration of BLU9931, BYL719 or BKM120 significantly decreased proliferation
316 of MDA-MB-453 cells (Fig. 3G,H). However, combining BLU9931 with BYL719 (or BKM120)
317 exhibited a similar effect to single inhibitor treatment (Fig. 3G,H), consistent with effects on AKT
318 activation.
319
320 Next, we simulated the combined effect of BLU9931 and AKT inhibition (AKTi) on pAKT.
321 Unlike PI3Ki, model simulations predicted a complete elimination of BLU9931-induced pAKT
322 rebound by the co-administration of AKTi (Fig. 3I). To confirm this experimentally, we treated
323 MDA-MB-453 cells with BLU9931 and the AKT inhibitor MK2206 alone or in combination (Fig.
324 3J&S5) for 4 h and 24 h. Treatment with the BLU9931+MK2206 combination potently suppressed
325 pAKT at 24 h, consistent with our model prediction (Fig. 3I-J). Individual treatment with MK2206
326 also suppressed pAKT to a greater extent than BLU9931 alone at 4 h (Fig. 3J). This marked
327 suppression of pAKT with MK2206 is expected because AKT is inhibited directly, unlike the
328 situation with PI3K inhibitors, which inhibit PI3K upstream of AKT. Consistent with these data,
329 treatment with MK2206 significantly decreased proliferation of MDA-MB-453 cells (Fig. 3K).
330 Moreover, combining BLU9931 with MK2206 was significantly more effective in blocking cell
331 proliferation than either agent alone (Fig. 3K).
332
333 Collectively, our results indicate that the efficacy of BLU9931 is limited by the 'bounce-back' of
334 AKT which can be blocked by an AKT inhibitor but not PI3K inhibitors. The combination of
335 BLU9931 with MK2206 is more effective than individual treatments in inhibiting cell proliferation
336 because the former drug suppresses other signalling pathways (e.g. ERK), while the latter inhibits
337 AKT, leading to an overall suppression of downstream signalling.
338
339 **Upregulated RTKs in parental and BLU9931-resistant MDA-MB-453 cells**
340 While FGFR4 inhibition results in dynamic reactivation of AKT, the network rewiring mechanism
341 that underpins this remains unclear. Since such signalling bounce-back is often caused by loss of
342 negative feedback signals to upstream network nodes including specific RTKs (30-32), we asked
343 if this was the case in our system. To explore this, we extended our model simulation readouts
344 beyond pAKT and simulated the response of pIGF1R, pIRS and pErbBs to BLU9931 in a time-
345 and dose-dependent manner (Fig. 4A and Fig S6), as these proteins are under regulation of multiple
346 negative feedback loops (Fig. 2A). Time-course simulations predicted a strong and significant
347 upregulation of pIGF1R, pIRS and pErbB at 24 h following BLU9931 treatment, both at low
348 (10nM) and high (100nM) doses (Fig. 4A). Moreover, the dose-dependent simulations suggested
349 that higher BLU9931 concentrations led to stronger upregulation of these proteins (Fig S6), as
350 seen previously for pAKT (Figs. 3A-D). These model predictions led us to hypothesize that
351 FGFR4 inhibition remodelled the RTK network in TNBC cells, which caused pAKT rebound and
352 compromised the inhibitory effect of BLU9931 on cell proliferation.
353

354 To test this hypothesis and the model predictions, we first characterized the temporal expression
355 and phosphorylation of particular RTKs in MDA-MB-453 cells after 1 h and 24 h BLU9931
356 treatment. In agreement with model predictions, we observed a marked upregulation of pIGF1R,
357 pIRS and pErbB2-3 at 24 h compared to the vehicle control or 1 h treatment (Fig. 4B), and as
358 predicted, these upregulations were more pronounced at the higher concentration of BLU9931
359 (100nM vs. 10nM, Fig. 4B).
360
361 In addition to investigating the short-term remodelling of the FGFR4 network in response to
362 BLU9931, we also interrogated the long-term effects of treatment with this drug. To this end,
363 MDA-MB-453 cells were exposed to BLU9931 for at least 3 months until visible colonies formed,
364 allowing isolation of resistant cells (see Material and Methods). Compared to parental cells, long-
365 term drug-treated cells were not significantly growth-inhibited by 10 nM BLU9931, and the effect
366 of 100 nM drug treatment was markedly reduced (Fig. 4C,D).
367
368 Since FGFR4 kinase domain gatekeeper mutations are an important mechanism for development
369 of resistance to anti-FGFR4 small molecule drugs (27), we first subjected the FGFR4 kinase
370 domain in parental and long-term BLU9931 cells to DNA sequencing. However, FGFR4
371 gatekeeper mutations were not detected (Fig S7). Next, we characterized the expression profile of
372 FGFR4 signalling network components. Interestingly, similar to parental cells treated with
373 BLU9931 for 24 h, long-term BLU9931-treated cells demonstrated a marked upregulation of
374 pAKT, pIGF1R, pIRS and pErbB2-3 (Fig. 4B). Of note, levels of phosphorylated GSK3α/β and
375 pY1248 ErbB2 were higher in the long-term BLU9931-treated cells than in parental cells treated
376 for 24 h with BLU9931 (Fig. 4B). Consequently, while increased activation of particular RTKs
377 induced by 24 h BLU9931 treatment is maintained in the long-term drug-refractory cells,
378 additional changes occur that likely underpin the long-term resistance to BLU9931. These
379 integrative data highlight upregulated RTKs and other signalling nodes that represent potential
380 targets for combination treatments with BLU9931, a concept that is formally addressed in the
381 following section.
382
383 **Model prediction and validation of synergistic drug combinations co-targeting FGFR4**
384 While complex interactions within the FGFR4 network pose significant challenges to the
385 identification of effective drug combinations (32, 33), our computational model provides a
386 powerful framework for the systematic prediction of nodes that could be targeted along with
387 FGFR4 to overcome adaptive resistance to anti-FGFR4 monotherapy. To explore this, we
388 simulated *in silico* the efficacy of 20 possible pair-wise drug combinations co-targeting FGFR4
389 and each of 20 other network nodes using our model (Fig. 5A). The performance of each
390 combination was theoretically evaluated by computing a coefficient of drug interaction (CDI, see
391 Materials and Methods for details) that quantifies how well it suppresses cell proliferation in
392 comparison to the single-drug treatments (Fig. 5A). CDI <1, =1, >1 indicates synergistic, additive
393 or antagonistic effects, respectively; and its value signifies the magnitude of

394 synergism/antagonism. Sorting the CDI scores allowed us to rank and prioritise the drug
395 combinations according to their predicted synergistic effects (Fig. 5A).

396 The model predicted that combined inhibition of FGFR4 and the ErbB receptors represented the
397 most synergistic combination, followed by co-inhibition of FGFR4 and AKT, PDK1 or IGF1R
398 (Fig. 5A). In contrast, co-targeting FGFR4 and PI3K or FGFR4 and MEK/SHP2 was predicted to
399 be not synergistic. The fact that the model correctly predicted the synergistic effect of co-targeting
400 FGFR4 and AKT, but not PI3K (Fig. 3), lends support to the validity of our approach. In addition,
401 the presence of ErbBs and IGF1R amongst the top predicted synergistic co-targets is consistent
402 with our data demonstrating upregulation of these RTKs in response to acute FGFR4 inhibition
403 and in the long-term resistant cells (Fig. 4).

404 Since ErbBs were predicted to be the most synergistic FGFR4 co-target, we next aimed to validate
405 this prediction. To suppress the activity of ErbB2, the long-term BLU9931-maintained cells were
406 treated with Lapatinib, with 100 nM selected as the most appropriate dose (Fig. 5B,C). Lapatinib
407 treatment alone had no effect on either parental or resistant cells (Fig. 5D-G). In cells maintained
408 long-term in 10 nM BLU9931, the combination treatment with Lapatinib restored growth
409 inhibition (Fig. 5F). At 100 nM BLU9931, the combination treatment caused cell death in both
410 parental (Fig. 5E) and resistant cells (Fig. 5G). These results indicate that although the parental
411 cells exhibit similar RTKs upregulated 24 h post-BLU9931 treatment, the long-term BLU9931-
412 maintained cells may be more dependent on ErbB2, consistent with the presence of enhanced
413 Y1248 phosphorylation. Taken together, our computational analyses and experimental validation
414 demonstrate that co-targeting ErbB2 can synergistically enhance the efficacy of FGFR4 inhibition
415 in MDA-MB-453 TNBC cells.
416

417 **Model-based identification of network connections underpinning pAKT rebound**

418 Our results so far implicate the upregulation of RTKs such as particular ErbBs and IGF1R in the
419 reactivation of pAKT after FGFR4 inhibition, yet the precise network interactions that mediate the
420 pAKT rebound remain unclear. In this section, we leveraged the mechanistic nature of our model
421 to computationally interrogate which regulatory links are essential in mediating pAKT's rebound
422 pattern. First, we performed model sensitivity analysis where we systematically blocked the
423 network links by inhibiting the corresponding kinetic parameter values one at a time by 75%, and
424 simulated the resulting pAKT time-course following BLU9931 treatment (Fig. 6A). Visual
425 inspection indicated significant changes to the pAKT dynamics, which were highly specific to the
426 perturbed parameters (Fig. 6A). To assess these changes quantitatively, we defined two general
427 metrics characterising a typical drug-induced rebound dynamic pattern: (i) a *'rebound'* (RB) and
428 an *'early drug effect'* (EDE), deriving from 3 basic measures: B = the pre-treated level, C = the
429 minimal level, and the rebound steady-state level (Y), as shown in Fig. 6B. Accordingly, a higher
430 RB score reflects a more dramatic rebound and a higher EDE score means the drug effect is more
431 potent initially. We then applied these scores to the sensitivity analysis of kinetic parameters
432 controlling the pAKT rebound dynamics (Fig. 6C). We found that for > one-third of the model

433 parameters, blocking them significantly decreased the RB score, suggesting a positive role for
434 these links in mediating pAKT rebound (Fig. 6C). In contrast, almost a half of the remaining
435 parameters had the opposite effect, while the other half did not significantly influence the RB score
436 (Fig. 6C). Interestingly, there was generally an inverse correlation between the RB and EDE scores
437 (Fig. 6C and S8), indicating that parameters that increased pAKT rebound also tended to decrease
438 the initial drug effect on pAKT, as seen visually in Fig. 6A.
439
440 Next, to provide greater insights into the parameter effects on the RB and EDE scores, we
441 performed a clustering analysis of these scores and classified the parameters into two distinct
442 groups with opposing effects on pAKT response (Fig. 6D). Blocking the parameters in group A
443 led to reduced pAKT rebound (also a lower steady state) and enhanced the early inhibitory effect
444 of the drug on pAKT (Fig. 6E, blue curves); while blocking those in group B potentiated pAKT
445 rebound and also blunted the initial drug effect on pAKT (Fig. 6E, red curves). Mapping these
446 parameters onto the network schematic diagram highlighted specific network interactions,
447 including feedback loops and cross-pathway connections that modulate the pAKT response in
448 opposite fashions (Fig. 6F).
449
450 **Diverse pAKT/pERK response profiles following FGFR4 inhibition across cancer cell lines**
451 Previously, we determined that cell-to-cell variation in protein expression levels is a major source
452 of signalling response heterogeneity (28). This led us to hypothesize that FGFR4 inhibitor-induced
453 signalling dynamics may be dictated by the protein expression profile across specific cancer cell
454 types. To address this hypothesis, we obtained protein expression data for 350 different cancer cell
455 lines of diverse tissue origins from the Cancer Cell Line Encyclopaedia (CCLE) consortium (35),
456 and used these as inputs to customize our MDA-MB-453 model, generating 350 models that reflect
457 the specific protein expression profile of each cell type (see Fig S9A for detailed workflow). Using
458 these cell type-specific models, we simulated the temporal profiles of pAKT and pERK in response
459 to FGFR4 inhibition in each cell type. Hierarchical clustering analysis revealed a remarkable
460 heterogeneity in the response of these outputs, ranging from no significant change to strong
461 rebound to straight increase patterns for pAKT (Fig. 7A), while pERK predominantly displayed
462 rebound or monotonic decrease patterns (Fig. 7B). By defining 3 types of possible composite
463 patterns: REB (rebound), INC/NOC (increase/no significant change) or DEC (decrease), we
464 further classified the cell lines into subgroups with distinct response profiles of pAKT-pERK,
465 resulting in 4 major subgroups: REB-REB (Group 1), INC/NOC-REB (Group 2), REB-DEC
466 (Group 3) and INC/NOC-DEC (Group 4) (Fig. 7C and Fig. S9B). Interestingly, FGFR4i induced
467 pERK rebound in about one-third of the cell lines (34%), indicating that re-activation of ERK
468 represents a salient response feature post FGFR4i treatment in a subset of cell types that likely
469 blunts the treatment effect. In addition, while pAKT displayed rebound in about 9% of the cell
470 lines, our simulations suggest that in the remaining cell lines (91%) FGFR4i either did not
471 significantly affect or even induced a straight increase of pAKT, indicating bounce-back may not
472 be the only dynamic feature underpinning the ability of AKT to mediate FGFR4i resistance. In

473 particular, nearly two-third (63%) of the cell lines displayed concomitant pAKT increase/no
474 change and pERK decrease, and 7% exhibited rebound in both pAKT and pERK (Fig. 7C).
475
476 We next asked whether it is possible to switch from one group to another by modulating particular
477 network components. To address this, we utilised the MDA-MB-453 model (representing Group
478 1), and systematically perturbed the expression levels of every network component, in order to
479 determine whether we could convert the pAKT response from REB to INC (Group 1 → Group 2)
480 or pERK response from REB to DEC (Group 1 → Group 3). This perturbation analysis showed
481 that either downregulation of FGFR4, FRS2, Grb2 or Ras, or upregulation of CBL, IGF1R, IRS
482 or PI3K switched pAKT from rebound to increase (Fig. 7D and Fig. S10); while downregulation
483 of ERK, MEK, Raf, Ras or upregulation of AKT switched pERK from rebound to decrease (Fig.
484 7E and Fig. S10). Overall, these findings highlight the remarkable plasticity of signalling networks
485 and the need to embrace network context in the analysis of drug-induced network remodelling.
486
487 **Alternative network rewiring following selective FGFR4 inhibition in Hep3B cells**
488 Our model-based analysis above predicted different subgroups of cancer cell types with
489 contrasting response patterns for pAKT-pERK that likely compromise the effect of FGFR4
490 inhibition. Group 1 is exemplified by the MDA-MB-453 cell line (Fig. 1D). To further test the
491 model prediction and the validity of Group 2, we identified the HCC cell line Hep3B to be a
492 member of this group (Fig. S11A). Hep3B displays active FGFR4 signalling due to gene
493 amplification of the FGFR4 ligand, FGF19 (9).
494
495 To investigate the network rewiring mechanisms following anti-FGFR4 treatment in Hep3B, we
496 exposed these cells to H3B-6527 (9). Cells treated with this drug at concentrations of 5nM or
497 higher demonstrated a marked decrease in pFRS2 and pERK after 1 h (Fig. S11B). Consistent with
498 our prediction for the behaviour of Group 2, cells treated with H3B-6527 demonstrated an early
499 and temporally increasing rebound of pERK levels despite the on-target drug effect evident by the
500 durable suppression of pFRS2 (Fig. 7F and S11B). In addition, pAKT displayed no significant
501 change following H3B-6527 treatment in Hep3B (Fig. S11B, C), which is also in accordance with
502 Group 2 behaviour. These dynamic responses are in contrast to the patterns observed in MDA-
503 MB-453, where strong pAKT rebound is a salient property and early pERK rebound is absent.
504 Together, these data confirm the validity of group 2 and validate Hep3B as an example member
505 of this group.
506
507 The rebound recovery of pERK signals after H3B-6527 treatment suggested that co-targeting ERK
508 may restore the sensitivity of Hep3B cells to H3B-6527. To test this, we first determined the
509 appropriate concentration of Trametinib, a MEK inhibitor that targets the MAPK signalling
510 pathway upstream of ERK, for combination treatments. Trametinib at 5nM or higher decreased
511 pERK in Hep3B cells (Fig. S11D). Next, Hep3B cells were treated with H3B-6527 and
512 Trametinib, alone or in combination. While both H3B-6527 and Trametinib alone both

513 significantly decreased Hep3B cell proliferation (Fig. 7G-H), the combination treatment resulted
514 in a significantly greater effect (Fig. 7H). This indicates that the efficacy of H3B-6527 is improved
515 by blocking the ERK 'bounce-back' and highlights this combination treatment as a promising
516 therapeutic approach for HCC.
517
518
519 **Discussion**
520 Tumour cells evade targeted cancer therapies via an elaborate repertoire of resistance mechanisms.
521 One common theme involves rapid and dynamic rewiring of signalling pathways in order to bypass
522 the drug blockade (15, 16, 29-31). Network adaptation occurs across different cancer types in
523 preclinical models (16, 32, 33) as well as in patients (34), highlighting adaptive resistance as a
524 major challenge to the clinical success of cancer therapies. However, pathway crosstalk and
525 feedback render signalling responses to targeted treatment highly non-linear (35, 36), making it
526 difficult to predict their behaviour. An in-depth understanding of adaptive resistance requires an
527 ability to integrate signalling pathways in unified predictive frameworks and to describe their
528 dynamics quantitatively at a system level. In this study, we developed a detailed ODE-based
529 dynamic model of the FGFR4 signalling network that incorporates major cell-surface receptors
530 and key convergent signalling pathways. Rigorous model calibration and validation using time-
531 resolved drug perturbation data from MDA-MB-453 TNBC cells allowed the model to be
532 specifically tailored to this cell type and ensured its validity. To our knowledge, this represents the
533 first instance of a detailed and experimentally-validated model of the FGFR signalling network. In
534 addition, we utilized our systems-based approach to characterise adaptive resistance to anti-
535 FGFR4 inhibition in FGFR4-driven cancers, and identified combinatorial strategies that overcome
536 drug resistance.
537
538 Combining model simulation and experimental analysis, we demonstrated that in MDA-MB-
539 453 cells, inhibition of FGFR4 by selective inhibitors led to a strong reactivation of the pro-
540 survival protein AKT. As AKT signalling is critical for FGF19-FGFR4 mediated growth in breast
541 cancer cells (37), this 'bounce-back' of AKT signal indicates that the FGFR4 network is
542 dynamically rewired to overcome FGFR4 inhibition. These results further imply that a
543 combination of FGFR4 and PI3K or AKT inhibitors may be a more effective therapeutic strategy
544 than targeting FGFR4 alone. However, our model simulations predicted that co-targeting of
545 FGFR4 and AKT, but not PI3K, would effectively eliminate the pAKT rebound. This was
546 subsequently validated experimentally, where the combination of BLU9931 with an AKT inhibitor
547 potently suppressed AKT activation rebound and cell proliferation. Consistent with these data, the
548 selective FGFR1-3 inhibitor AZD4547 and AKT inhibitor AZD5363 exhibited additive effects
549 against FGFR1-expressing prostate cancer *in vitro* and *in vivo* (38). Furthermore, since mTOR
550 signals downstream of AKT, mTOR inhibitors may also be promising in combination therapy. In
551 support of this, the mTOR inhibitor AZD2014 in combination with AZD4547 demonstrated

552 tumour growth attenuation in tumour xenografts generated from FGFR1-dependent lung cancer
553 cells (39).
554
555 Combinatorial targeting of FGFR4 is a relatively understudied area, and most work has focused
556 on combining FGFR4 inhibition with radio/chemotherapeutics (40, 41). In order to expedite
557 identification of novel combination treatments that target FGFR4 together with other RTKs and
558 signalling proteins, we exploited the mechanistic and quantitative nature of our model to predict
559 the effect of 20 possible pair-wise drug combinations co-targeting FGFR4 and other network
560 components in a systematic and unbiased manner. Among the different components, ErbB
561 receptors were predicted to be the most synergistic FGFR4 co-target. This was confirmed
562 experimentally, where combined inhibition of FGFR4 and ErbB2 using BLU9931 and Lapatinib,
563 but not administration of the individual drugs, resulted in death of both the parental and long-term
564 BLU9931-resistant cells. These findings are consistent with the activation of alternative RTKs as
565 an escape mechanism previously reported in FGFR-resistance models (42, 43). For example,
566 FGFR3-dependent bladder cancer cell lines developed resistance to the pan-FGFR inhibitor
567 BGJ398 by switching receptor signalling to ErbB2 or ErbB3, and here the dual inhibition of
568 FGFR3 and ErbB activity resulted in increased cell death (42). Also, unbiased screening using
569 pTyr RTK arrays identified high levels of pEGFR and pErbB2 in two FGFR-dependent basal-like
570 breast cancer tumour xenografts after FGFR inhibition (44), and combining the pan-ErbB inhibitor
571 AEE788 and multi-kinase pan-FGFR inhibitor Dovitinib resulted in inhibition of the downstream
572 FRS2-ERK and AKT pathways and tumour growth and metastasis (44).
573
574 Our model-based perturbation analysis also identified points of network interference that could
575 switch the response behaviour from one pattern to another, e.g. from a rebound in activation of
576 pAKT to a progressive increase, highlighting how the plasticity of signalling networks provides a
577 mechanism to modulate drug response. It is likely that cancer cells exploit this capability to switch
578 from a drug-sensitive to a drug-resistant state. On the flip side, a detailed understanding of network
579 behaviour and adaptability will aid the design of novel therapeutic strategies to counter drug-
580 induced re(activation) of pro-growth signalling, e.g. by converting (re)activation of pAKT/pERK
581 to a reduction in activity. Overall, these findings highlight integrative network modelling as a
582 powerful approach to analyse and predict network changes required for manipulating specific
583 signalling behaviours.
584
585 It has become increasingly appreciated that the mechanisms underpinning adaptive resistance
586 can be highly heterogeneous and context-specific, even in response to the same drug compounds
587 (45). This is primarily driven by variation in protein expression and/or mutational profiles
588 observed across and within different cancer cell types, resulting in context-specific differences in
589 feedback and crosstalk strengths that impact on drug response (19, 28). For example, BRAF
590 inhibition by vemurafenib is effective in BRAF-mutant melanoma but not colorectal cancer,
591 reflecting higher EGFR expression in the latter cancer type. Consequently, in colorectal cancer,

592 vemurafenib induces feedback activation of the EGFR that allows continued MAPK signalling
593 and cellular proliferation (46). However, due to the complexity of signalling networks and lack of
594 predictive models, our ability to predict context-dependent network rewiring remains limited.
595 Here, we incorporated publicly available protein expression data from hundreds of cancer cell
596 types to adjust the state variables of our model, enabling us to adapt the model to diverse cellular
597 contexts and identify four major response patterns for pAKT and pERK. Amongst the cell types
598 exhibiting increase/no change pattern in AKT activation in combination with ERK rebound, we
599 identified and experimentally validated the HCC cell line Hep3B. Importantly, co-targeting
600 FGFR4 and MEK (upstream of ERK) in Hep3B cells markedly enhanced inhibition of cell
601 proliferation. Together, our results highlight co-targeting FGFR4 and ERK as a novel precision
602 treatment strategy for HCC.
603
604 Overall, through an integrative approach we have identified mechanisms of FGFR4 pathway
605 rewiring and identified potential combination targeted therapies with increased efficacy for
606 FGFR4-driven TNBC and HCC cancers. Given that co-targeting FGFR4 and ErbB2 was
607 particularly effective, there is significant potential in expanding this targeted treatment strategy to
608 other breast cancer subtypes of poor prognosis, including luminal B and HER2 breast cancers.
609 Finally, the computational models and integrative systems-based approach utilised provide a
610 valuable foundation for future investigation of network rewiring and adaptive resistance related to
611 targeting of other RTKs in breast cancer as well as other malignancies.
612
613
614 **References**

615 1. I. S. Babina, N. C. Turner, Advances and challenges in targeting FGFR signalling in
616 cancer. *Nat Rev Cancer* **17**, 318-332 (2017).
617 2. Y. Loriot *et al.*, Erdafitinib in Locally Advanced or Metastatic Urothelial Carcinoma. *N*
618 *Engl J Med* **381**, 338-348 (2019).
619 3. K. M. Levine, K. Ding, L. Chen, S. Oesterreich, FGFR4: A promising therapeutic target
620 for breast cancer and other solid tumors. *Pharmacology & Therapeutics* **214**, 107590
621 (2020).
622 4. K. M. Levine *et al.*, FGFR4 overexpression and hotspot mutations in metastatic ER+
623 breast cancer are enriched in the lobular subtype. *npj Breast Cancer* **5**, 19 (2019).
624 5. D. Meijer *et al.*, Fibroblast growth factor receptor 4 predicts failure on tamoxifen therapy
625 in patients with recurrent breast cancer. *Endocr Relat Cancer* **15**, 101-111 (2008).
626 6. S. Garcia-Recio *et al.*, FGFR4 regulates tumor subtype differentiation in luminal breast
627 cancer and metastatic disease. *J Clin Invest* **130**, 4871-4887 (2020).

628 7. N. J. Chew *et al.*, Evaluation of FGFR targeting in breast cancer through interrogation of
629 patient-derived models. *Breast Cancer Res* **23**, 82 (2021).
630 8. E. T. Sawey *et al.*, Identification of a therapeutic strategy targeting amplified FGF19 in
631 liver cancer by Oncogenomic screening. *Cancer Cell* **19**, 347-358 (2011).
632 9. J. J. Joshi *et al.*, H3B-6527 Is a Potent and Selective Inhibitor of FGFR4 in FGF19-
633 Driven Hepatocellular Carcinoma. *Cancer Res* **77**, 6999-7013 (2017).
634 10. M. Hagel *et al.*, First Selective Small Molecule Inhibitor of FGFR4 for the Treatment of
635 Hepatocellular Carcinomas with an Activated FGFR4 Signaling Pathway. *Cancer Discov*
636 **5**, 424-437 (2015).
637 11. R. D. Kim *et al.*, First-in-Human Phase I Study of Fisogatinib (BLU-554) Validates
638 Aberrant FGF19 Signaling as a Driver Event in Hepatocellular Carcinoma. *Cancer*
639 *Discovery* **9**, 1696-1707 (2019).
640 12. E. D. Fleuren, L. Zhang, J. Wu, R. J. Daly, The kinome 'at large' in cancer. *Nat Rev*
641 *Cancer* **16**, 83-98 (2016).
642 13. P. Saraon *et al.*, Receptor tyrosine kinases and cancer: oncogenic mechanisms and
643 therapeutic approaches. *Oncogene* **40**, 4079-4093 (2021).
644 14. K. E. O'Reilly *et al.*, mTOR Inhibition Induces Upstream Receptor Tyrosine Kinase
645 Signaling and Activates Akt. *Cancer Research* **66**, 1500-1508 (2006).
646 15. S. Chandarlapaty *et al.*, AKT inhibition relieves feedback suppression of receptor
647 tyrosine kinase expression and activity. *Cancer Cell* **19**, 58-71 (2011).
648 16. J. S. Duncan *et al.*, Dynamic reprogramming of the kinome in response to targeted MEK
649 inhibition in triple-negative breast cancer. *Cell* **149**, 307-321 (2012).
650 17. T. Nakakuki *et al.*, Ligand-specific c-Fos expression emerges from the spatiotemporal
651 control of ErbB network dynamics. *Cell* **141**, 884-896 (2010).
652 18. S. Y. Shin *et al.*, The switching role of beta-adrenergic receptor signalling in cell survival
653 or death decision of cardiomyocytes. *Nat Commun* **5**, 5777 (2014).
654 19. S. Y. Shin, A. K. Muller, N. Verma, S. Lev, L. K. Nguyen, Systems modelling of the
655 EGFR-PYK2-c-Met interaction network predicts and prioritizes synergistic drug
656 combinations for triple-negative breast cancer. *PLoS Comput Biol* **14**, e1006192 (2018).
657 20. F. Reali, C. Priami, L. Marchetti, Optimization Algorithms for Computational Systems
658 Biology. *Frontiers in Applied Mathematics and Statistics* **3** (2017).

659 21. K. F. Man, K. S. Tang, S. Kwong, Genetic algorithms: concepts and applications [in
660 engineering design]. *IEEE Transactions on Industrial Electronics* **43**, 519-534 (1996).
661 22. S. Y. Shin *et al.*, The switching role of β-adrenergic receptor signalling in cell survival or
662 death decision of cardiomyocytes. *Nat Commun* **5**, 5777 (2014).
663 23. X. Li *et al.*, β-elemene sensitizes hepatocellular carcinoma cells to oxaliplatin by
664 preventing oxaliplatin-induced degradation of copper transporter 1. *Scientific Reports* **6**,
665 21010 (2016).
666 24. F. Liu, Y. Shang, S.-z. Chen, Chloroquine potentiates the anti-cancer effect of lidamycin
667 on non-small cell lung cancer cells in vitro. *Acta Pharmacol Sin* **35**, 645-652 (2014).
668 25. A. Roidl *et al.*, The FGFR4 Y367C mutant is a dominant oncogene in MDA-MB453
669 breast cancer cells. *Oncogene* **29**, 1543-1552 (2010).
670 26. N. J. Chew *et al.*, FGFR3 signaling and function in triple negative breast cancer. *Cell*
671 *Commun Signal* **18**, 13 (2020).
672 27. M. A. Hatlen *et al.*, Acquired On-Target Clinical Resistance Validates FGFR4 as a
673 Driver of Hepatocellular Carcinoma. *Cancer Discovery* **9**, 1686-1695 (2019).
674 28. D. Norris *et al.*, Signaling Heterogeneity is Defined by Pathway Architecture and
675 Intercellular Variability in Protein Expression. *iScience* **24**, 102118 (2021).
676 29. A. Chakrabarty, V. Sanchez, M. G. Kuba, C. Rinehart, C. L. Arteaga, Feedback
677 upregulation of HER3 (ErbB3) expression and activity attenuates antitumor effect of
678 PI3K inhibitors. *Proc Natl Acad Sci U S A* **109**, 2718-2723 (2012).
679 30. M. Will *et al.*, Rapid induction of apoptosis by PI3K inhibitors is dependent upon their
680 transient inhibition of RAS-ERK signaling. *Cancer Discov* **4**, 334-347 (2014).
681 31. C. Fedele *et al.*, SHP2 Inhibition Prevents Adaptive Resistance to MEK Inhibitors in
682 Multiple Cancer Models. *Cancer Discov* **8**, 1237-1249 (2018).
683 32. C. G. Cremers, L. K. Nguyen, Network rewiring, adaptive resistance and combating
684 strategies in breast cancer. *Cancer Drug Resistance* **2**, 1106-1126 (2019).
685 33. Michael J. Lee *et al.*, Sequential Application of Anticancer Drugs Enhances Cell Death
686 by Rewiring Apoptotic Signaling Networks. *Cell* **149**, 780-794 (2012).
687 34. J. S. Zawistowski *et al.*, Enhancer Remodeling during Adaptive Bypass to MEK
688 Inhibition Is Attenuated by Pharmacologic Targeting of the P-TEFb Complex. *Cancer*
689 *Discov* **7**, 302-321 (2017).

690 35. B. N. Kholodenko, Cell-signalling dynamics in time and space. *Nat Rev Mol Cell Biol* **7**,
691 165-176 (2006).
692 36. M. Ghomlaghi, A. Hart, N. Hoang, S. Shin, L. K. Nguyen, Feedback, Crosstalk and
693 Competition: Ingredients for Emergent Non-Linear Behaviour in the PI3K/mTOR
694 Signalling Network. *Int J Mol Sci* **22** (2021).
695 37. X. Zhao *et al.*, FGFR4 provides the conduit to facilitate FGF19 signaling in breast cancer
696 progression. *Molecular Carcinogenesis* **57**, 1616-1625 (2018).
697 38. S. Feng *et al.*, Combination treatment of prostate cancer with FGF receptor and AKT
698 kinase inhibitors. *Oncotarget* **8**, 6179 (2017).
699 39. K. R. Singleton *et al.*, Kinome RNAi screens reveal synergistic targeting of MTOR and
700 FGFR1 pathways for treatment of lung cancer and HNSCC. *Cancer research* **75**, 4398-
701 4406 (2015).
702 40. R. Turkington *et al.*, Fibroblast growth factor receptor 4 (FGFR4): a targetable regulator
703 of drug resistance in colorectal cancer. *Cell death & disease* **5**, e1046-e1046 (2014).
704 41. M. A. Ahmed *et al.*, Correction: Fibroblast growth factor receptor 4 induced resistance to
705 radiation therapy in colorectal cancer. *Oncotarget* **10**, 5385 (2019).
706 42. J. Wang *et al.*, Ligand-associated ERBB2/3 activation confers acquired resistance to
707 FGFR inhibition in FGFR3-dependent cancer cells. *Oncogene* **34**, 2167-2177 (2015).
708 43. M. T. Herrera-Abreu *et al.*, Parallel RNA interference screens identify EGFR activation
709 as an escape mechanism in FGFR3-mutant cancer. *Cancer discovery* **3**, 1058-1071
710 (2013).
711 44. A. Issa *et al.*, Combinatorial targeting of FGF and ErbB receptors blocks growth and
712 metastatic spread of breast cancer models. *Breast Cancer Research* **15** (2013).
713 45. D. L. Cunningham *et al.*, Differential responses to kinase inhibition in FGFR2-addicted
714 triple negative breast cancer cells: a quantitative phosphoproteomics study. *Sci Rep* **10**,
715 7950 (2020).
716 46. A. Prahallad *et al.*, Unresponsiveness of colon cancer to BRAF(V600E) inhibition
717 through feedback activation of EGFR. *Nature* **483**, 100-103 (2012).

718
719

720 **FIGURE LEGENDS**

721 **Figure 1. Effect of the FGFR4 inhibitor BLU9931 on FGFR4 downstream signalling**
722 **pathways and proliferation in the MDA-MB-453 cell line. (A)** Dose dependent effect of
723 BLU9931 on expression and activation of downstream signalling proteins 1 h post-treatment with
724 the indicated doses. **(B)** Quantification by densitometry of (A). Data were first normalised relative
725 to the actin control, then phosphorylated proteins were normalised to total protein, finally data
726 were expressed relative to DMSO control which was arbitrarily set at 1.0. **(C)** Effect of BLU9931
727 on proliferation in the FGFR4-positive MDA-MB-453 (upper panel) and FGFR4-negative control
728 MDA-MB-468 cell lines (lower panel). Cell proliferation was determined by direct cell counting.
729 Error bars: mean ± standard error of three biological replicates. ** indicates p-value of < 0.01 and
730 *** < 0.001, comparing individual BLU9931 concentrations to the DMSO vehicle control. **(D)**
731 Time course analysis of BLU9931 on FGFR4 downstream signalling pathways in the MDA-MB-
732 453 cell line. Expression and activation of downstream signalling proteins 1, 4, 8 and 24 h post-
733 treatment with 10 nM of BLU9931. U indicates untreated control, D indicates DMSO vehicle
734 control. Representative of three biological replicates.
735

736 **Figure 2. Development and calibration of a mathematical model of the FGFR4 signalling**
737 **network. (A)** A simplified schematic diagram depicting the network interactions included in the
738 FGFR4 model, consisting of major RTKs, converging downstream signalling pathways and key
739 feedback and crosstalk mechanisms. A detailed model reaction diagram is provided in Figure S2.
740 The full model reaction rates and ODEs are given in Supplemental Table S1-2. **(B)** Model fitting
741 to experimental data. Comparison of model simulation using best-fitted parameter sets (blue lines,
742 error bars: mean ± standard error, n=5) against experimental time-course and dose-response data
743 (red lines, error bars: mean ± standard error, n=3) demonstrate good agreement between simulation
744 and data. Data used for model calibration were quantified from Figures 1A,D.
745

746 **Figure 3. Co-inhibition of FGFR4 and AKT, but not PI3K, eliminates pAKT rebound and**
747 **suppresses MDA-MB-453 cell proliferation. (A-D)** Model prediction of phosphorylated AKT
748 (pAKT) dynamics in response to FGFR4 inhibitor BLU9931 and PI3Kα inhibitor BYL719 in
749 single or combination treatment. Error bars: mean ± standard error of five best-fitted parameter
750 sets. **(E)** Dose dependent effect of BLU9931 in combination with BYL719, pan-PI3K inhibitor
751 BKM120 on AKT phosphorylation in the MDA-MB-453 cell line. Activation of AKT was
752 characterized 1 h and 24 h post-treatment with the indicated doses in single or combination
753 treatment. U indicates untreated control, D indicates DMSO vehicle control. **(F)** Quantification by
754 densitometry of data in (E). The quantified data were normalised to DMSO control. **(G, H)** Parental
755 MDA-MB-453 cells were subjected to single inhibitor treatment or combinations of BLU9931 and
756 BYL719 (G) or BKM120 (H). Cell proliferation was determined by MTS assay. Error bars: mean
757 ± standard error of four biological replicates. ** indicates p-value of < 0.01. **(I)** Model prediction
758 of pAKT dynamics in response to FGFR4 and AKT inhibitors in single or combination treatments.
759 To model AKT inhibition, the parameter values associated with AKT catalytic activity were

760 inhibited by 90%. Error bars: mean ± standard error of five best-fitted parameter sets. **(J)** Dose
761 dependent effect of the FGFR4 inhibitor BLU9931 in combination with AKT inhibitor MK2206
762 on AKT phosphorylation in the MDA-MB-453 cell line. Activation of AKT was characterized 1
763 h and 24 h post-treatment with the indicated doses of single or combination treatment. U indicates
764 untreated control, D indicates DMSO vehicle control. **(K)** MDA-MB-453 cells were subjected to
765 single inhibitor treatment or a combination of BLU9931 and MK2206. Cell proliferation was
766 determined by MTS assay. Error bars: mean ± standard error of four biological replicates. *
767 indicates p-value of < 0.05, ** < 0.01, *** < 0.001.
768
769 **Figure 4. Identification of upregulated RTKs in parental and BLU9931-resistant MDA-MB-**
770 **453 cells. (A)** Model prediction of the dynamic responses of phosphorylated RTKs, predicting they
771 are temporally upregulated following BLU9931 treatment in parental MDA-MB-453 cells. Error
772 bars: mean ± standard error of five best-fitted parameter sets. **(B)** Expression and activation of
773 RTKs and FGFR4 downstream signalling proteins at 1 and 24 h post-treatment with the indicated
774 BLU9931 concentrations in parental MDA-MB-453 cells, compared with long-term (LT)
775 BLU9931 MDA-MB-453 cells. The latter were harvested 24 h post-seeding. **(C-D)** The
776 proliferation of parental and long-term MDA-MB-453 cells treated with DMSO vehicle control,
777 10 nM (C) or 100 nM BLU9931 (D). Cell proliferation was determined by MTS assay. Error bars:
778 mean ± standard error of six biological replicates. ** indicates p-value of < 0.01, *** < 0.001.
779
780 **Figure 5. Model prediction of synergistic drug combinations and experimental validation.**
781 **(A)** *In silico* prediction of the effect of 20 possible pair-wise drug combinations co-targeting
782 FGFR4 and various network components, assessed using a drug synergy score (see Materials and
783 Methods for detail). Error bars: mean ± standard error of five best-fitted parameter sets. **(B, C)**
784 Dose dependent effect of Lapatinib on the expression and phosphorylation of ErbB2 in long-term
785 10 nM (B) or 100 nM BLU9931 MDA-MB-453 cells (C). **(D-G)** Parental (D, E) and long-term 10
786 nM or 100 nM BLU9931 (F, G) MDA-MB-453 cells were subjected to single inhibitor or
787 combination treatment of BLU9931 and Lapatinib at the indicated doses. Cell proliferation was
788 determined by MTS assay. Error bars: mean ± standard error of three biological replicates. *
789 indicates p-value of <0.05, ** < 0.01, *** < 0.001.
790
791 **Figure 6. Model-based sensitivity analysis and identification of network architecture**
792 **controlling pAKT rebound. (A)** A 3D plot showing *in silico* simulation of the temporal
793 phosphorylated AKT dynamics in response to FGFR4 inhibition, as each of the model kinetic
794 parameters was inhibited individually (by 75% of the nominal value). The pAKT dynamics of the
795 intact (non-perturbed) model is highlighted in white as control. The pAKT time profiles were
796 averaged across five best-fitted parameter sets. **(B)** Illustration of the general quantitative metrics:
797 *rebound* (RB) and *early drug effect* (EDE) scores, which characterise a typical rebound response,
798 here depicted for the BLU9931-induced pAKT dynamics as an example. These metrics are derived
799 from several basic measures: B: pre-treated (basal) pAKT level; C: the minimal level of pAKT

following drug treatment; and Y: the steady-state level of pAKT after drug treatment. **(C)** Sensitivity analysis results displaying the effect of systematically blocking each of the model kinetic parameters (by reducing the nominal values by 75%) on the RB and EDE scores of the BLU9931-induced pAKT response, relative to the control (no perturbation) condition. **(D)** A hierarchical clustering analysis of the RB and EDE scores obtained in (C), which identifies two major subgroups (group A and B) of the kinetic parameters. The scores are colour coded in log2 scale. **(E)** Simulated time profiles of pAKT response to FGFR4 inhibition when parameters of group A (blue lines) or B (red lines) were blocked, compared to the control (non-perturbed, black line) scenario. Blocking group A's parameters attenuates, while blocking group B's parameters intensifies pAKT rebound. **(F)** A simplified schematic highlighting the network links governed by the kinetic parameters belonging to group A (red lines) and B (blue lines).

Figure 7. Analysis of drug-induced pAKT/pERK response profiles across a large panel of cancer cell types. (A, B) Model prediction of pAKT and pERK time-course profiles in response to FGFR4 inhibition in 350 cancer cell lines using cell-type specific models generated by incorporating protein expression data from CCLE. **(C)** Classification of the cell lines into subgroups based on the response patterns of pAKT and pERK. INC: increase, DEC: decrease, REB: rebound, NOC: no change. **(D, E)** Modelling based identification of network perturbations (i.e. upregulation of the red or downregulation of the blue components) that may convert the pAKT response from a REB to an INC pattern (D); or the pERK response from a REB to a DEC pattern (E), demonstrating the marked plasticity of network-mediated drug response dynamics. **(F)** Time course analysis of treatment using the FGFR4 inhibitor H3B-6527 on FGFR4 downstream signalling pathways in the Hep3B cell line. Expression and activation of downstream signalling proteins were characterized 1, 4, 8 and 24 h post-treatment with 50 nM H3B-6527. U indicates untreated control, D indicates DMSO vehicle control. Representative of three biological replicates. **(G)** Effect of H3B-6527 treatment on proliferation of Hep3B cells. Cell proliferation was determined by MTS assay. Error bars: mean ± standard error of three biological replicates. * indicates p-value of < 0.05, ** < 0.01. **(H)** Parental Hep3B cells were subjected to single inhibitor treatments or a combination of H3B-6527 and Trametinib as indicated. Cell proliferation was determined by MTS assay. Error bars: mean ± standard error of four biological replicates. * indicates p-value of < 0.05, **< 0.01, *** < 0.001.

Figure 1

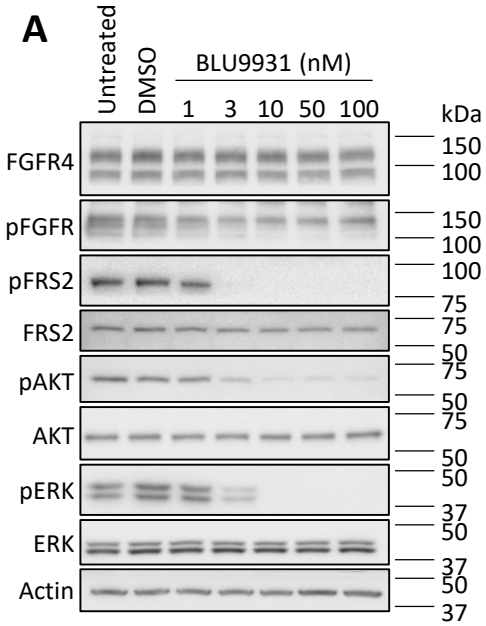
A
Untreated
DMSO
BLU9931 (nM)
1 3 10 50 100
kDa
FGFR4
pFGFR
pFRS2
FRS2
pAKT
AKT
pERK
ERK
Actin
150
100
150
100
100
75
75
50
75
50
75
50
50
37
50
37
50
37

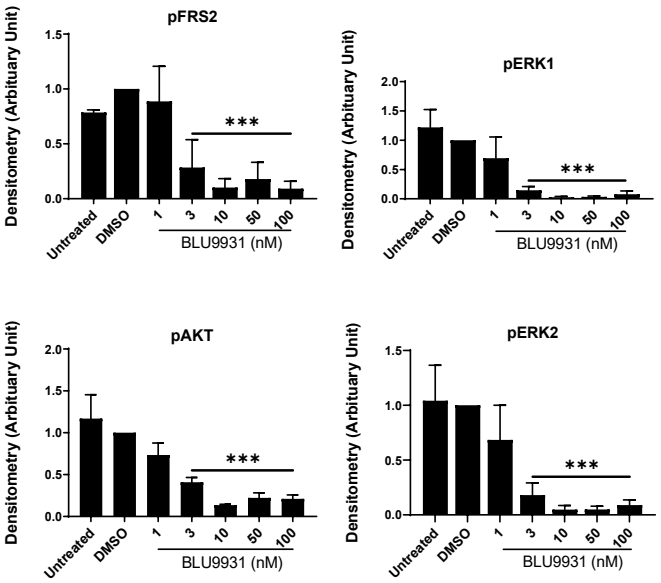
B
pFRS2
pERK1
pAKT
pERK2
Densitometry (Arbituary Unit)
Untreated
DMSO
1
3
10
50
100
BLU9931 (nM)
***

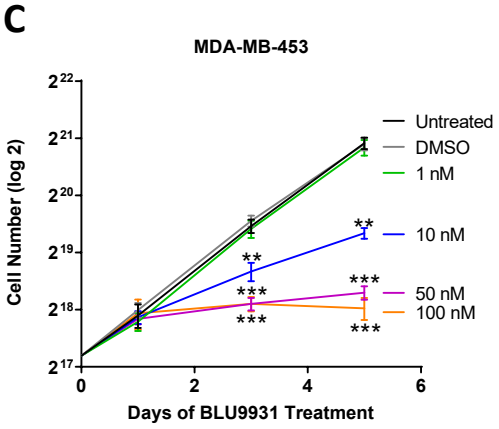
C
MDA-MB-453
Cell Number (log 2)
Days of BLU9931 Treatment
Untreated
DMSO
1 nM
10 nM
50 nM
100 nM
**
***

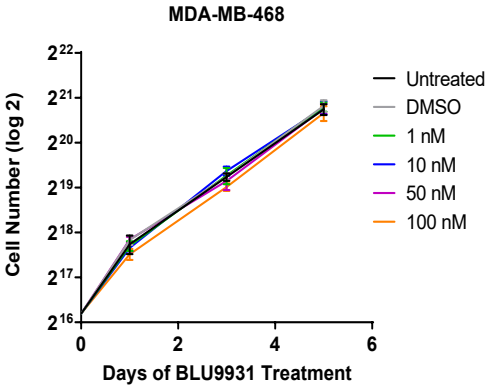
MDA-MB-468
Cell Number (log 2)
Days of BLU9931 Treatment
Untreated
DMSO
1 nM
10 nM
50 nM
100 nM

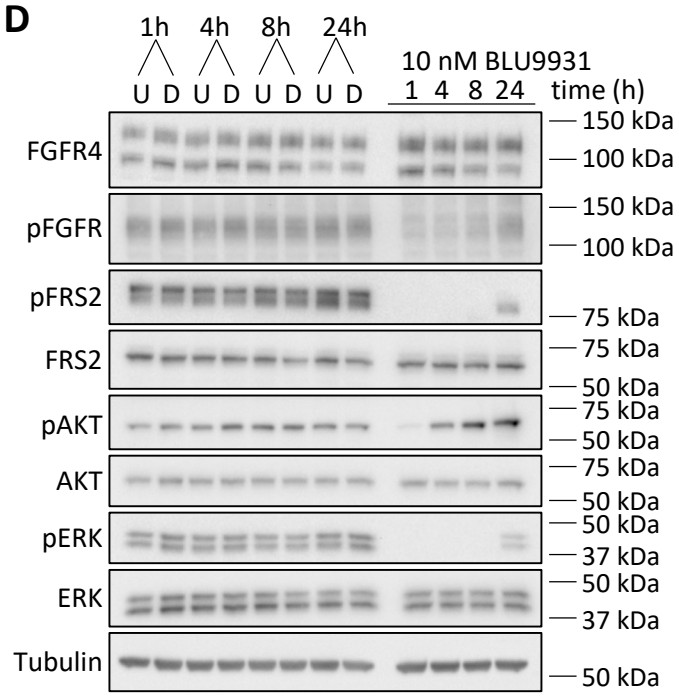
D
1h 4h 8h 24h
U D U D U D U D
10 nM BLU9931
1 4 8 24 time (h)
FGFR4
pFGFR
pFRS2
FRS2
pAKT
AKT
pERK
ERK
Tubulin
150 kDa
100 kDa
150 kDa
100 kDa
75 kDa
75 kDa
50 kDa
75 kDa
50 kDa
75 kDa
50 kDa
50 kDa
37 kDa
50 kDa
37 kDa
50 kDa

Figure 2

A

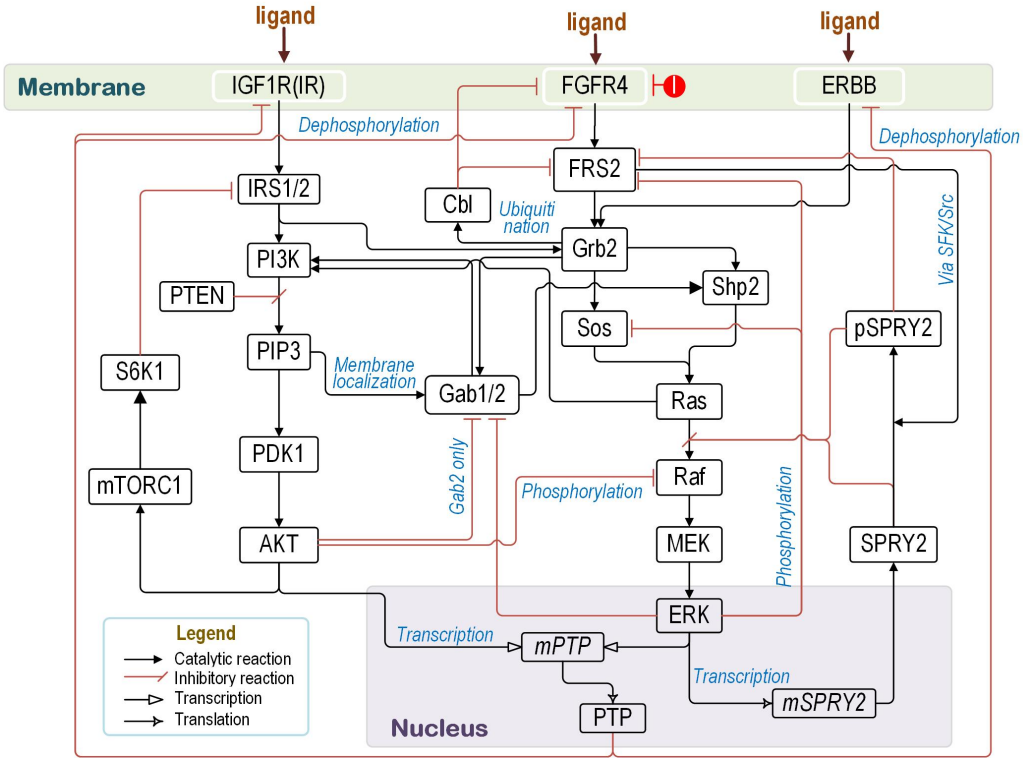
ligand
ligand
ligand
Membrane
IGF1R(IR)
FGFR4
ERBB
Dephosphorylation
Dephosphorylation
FRS2
IRS1/2
Cbl
Ubiquitination
Grb2
PI3K
Shp2
PTEN
Sos
pSPRY2
Via SFK/Src
PIP3
Membrane localization
S6K1
Gab1/2
Ras
PDK1
Gab2 only
Raf
mTORC1
Phosphorylation
Phosphorylation
AKT
MEK
SPRY2
ERK
Transcription
mPTP
Transcription
mSPRY2
PTP
Nucleus
Legend
Catalytic reaction
Inhibitory reaction
Transcription
Translation

B

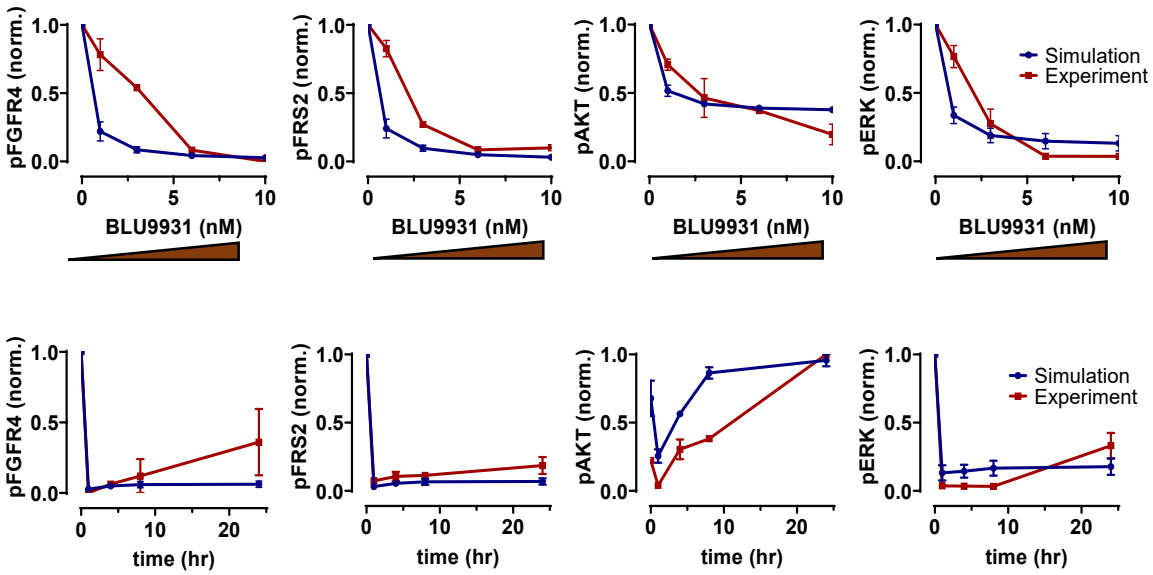
pFGFR4 (norm.)
pFRS2 (norm.)
pAKT (norm.)
pERK (norm.)
BLU9931 (nM)
Simulation
Experiment
time (hr)

Figure 3

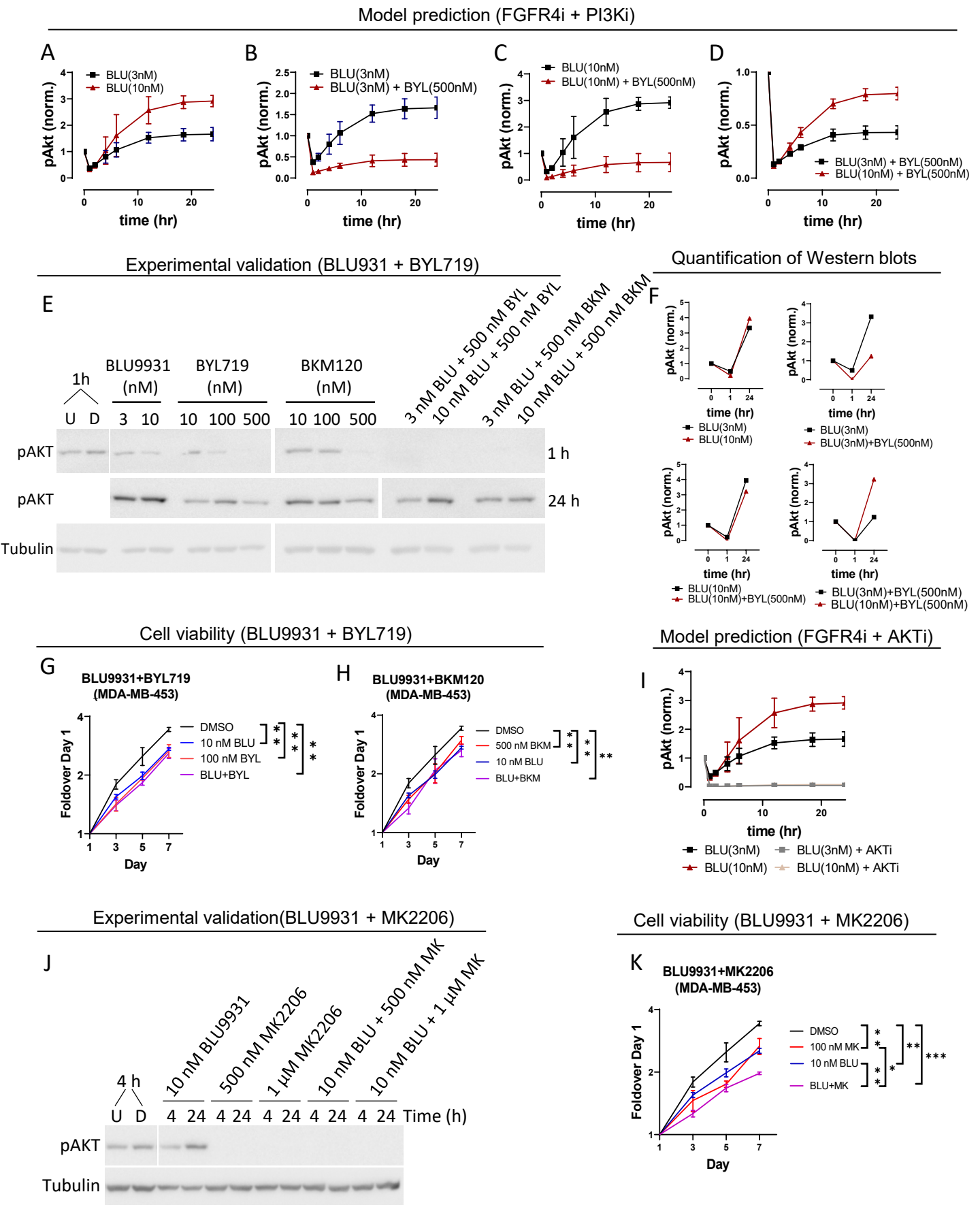
Model prediction (FGFR4i + PI3Ki)
A
BLU(3nM)
BLU(10nM)
pAkt (norm.)
time (hr)
B
BLU(3nM)
BLU(3nM) + BYL(500nM)
C
BLU(10nM)
BLU(10nM) + BYL(500nM)
D
BLU(3nM) + BYL(500nM)
BLU(10nM) + BYL(500nM)
Experimental validation (BLU931 + BYL719)
E
1h
U D
BLU9931 (nM)
3 10
BYL719 (nM)
10 100 500
BKM120 (nM)
10 100 500
3 nM BLU + 500 nM BYL
10 nM BLU + 500 nM BYL
3 nM BLU + 500 nM BKM
10 nM BLU + 500 nM BKM
pAKT
1 h
pAKT
24 h
Tubulin
Quantification of Western blots
F
BLU(3nM)
BLU(10nM)
BLU(3nM)+BYL(500nM)
BLU(10nM)+BYL(500nM)
Cell viability (BLU9931 + BYL719)
G
BLU9931+BYL719
(MDA-MB-453)
Foldover Day 1
Day
DMSO
10 nM BLU
100 nM BYL
BLU+BYL
H
BLU9931+BKM120
(MDA-MB-453)
DMSO
500 nM BKM
10 nM BLU
BLU+BKM
Model prediction (FGFR4i + AKTi)
I
BLU(3nM)
BLU(3nM) + AKTi
BLU(10nM)
BLU(10nM) + AKTi
Experimental validation(BLU9931 + MK2206)
J
10 nM BLU9931
500 nM MK2206
1 μM MK2206
10 nM BLU + 500 nM MK
10 nM BLU + 1 μM MK
4 h
U D
4 24 4 24 4 24 4 24 4 24 Time (h)
pAKT
Tubulin
Cell viability (BLU9931 + MK2206)
K
BLU9931+MK2206
(MDA-MB-453)
DMSO
100 nM MK
10 nM BLU
BLU+MK

Figure 4

A

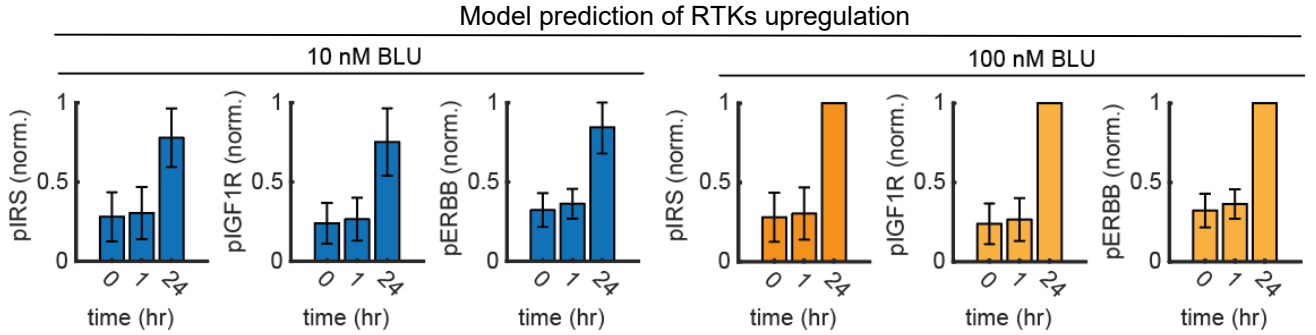

B

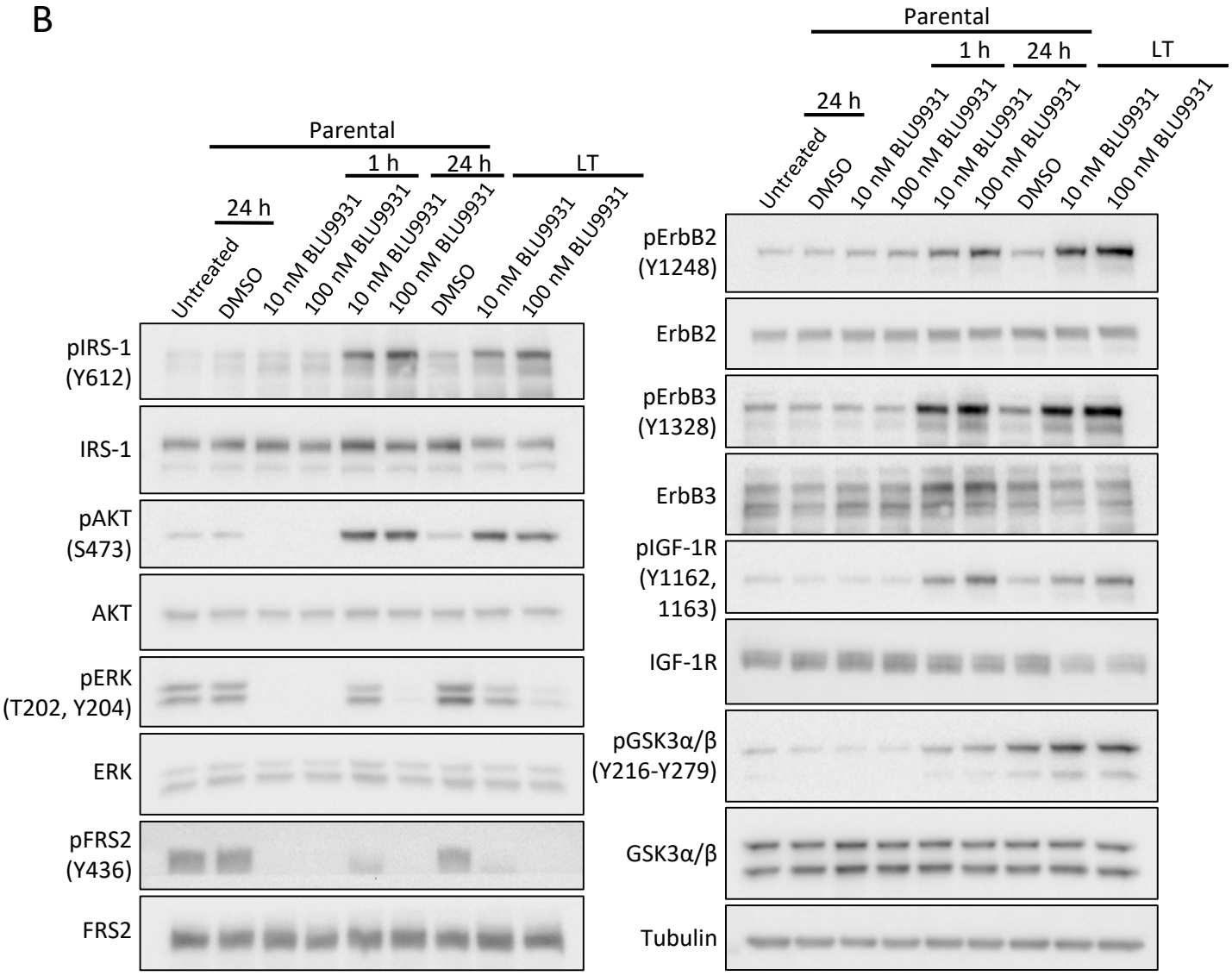

C

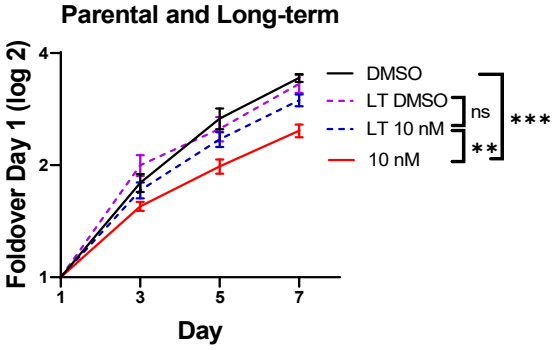

D

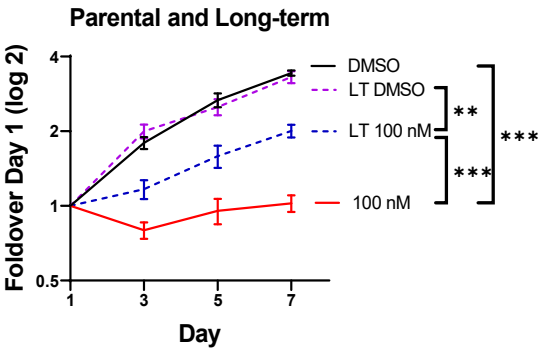

Figure 5

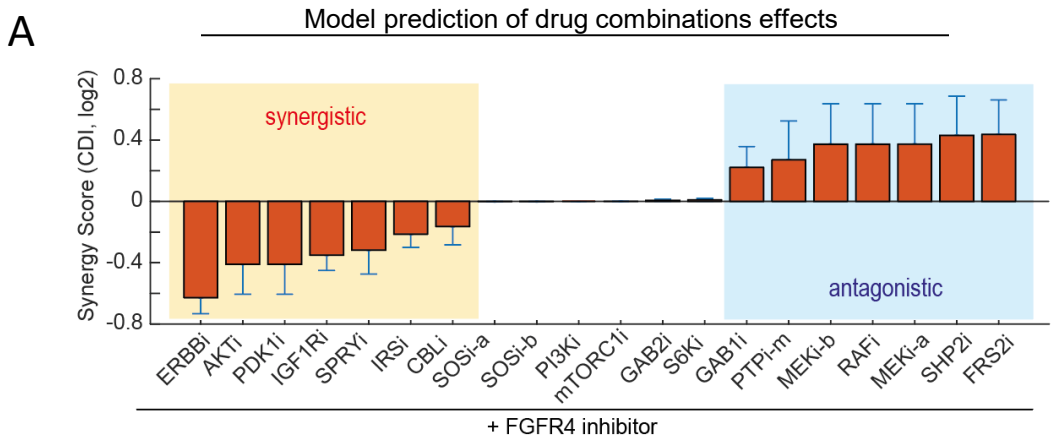
A
Model prediction of drug combinations effects
Synergy Score (CDI, log2)
0.8
0.4
0
-0.4
-0.8
synergistic
antagonistic
ERBBi
AKTi
PDK1i
IGF1Ri
SPRYi
IRSi
CBLi
SOSi-a
SOSi-b
PI3Ki
mTORC1i
GAB2i
S6Ki
GAB1i
PTPi-m
MEKi-b
RAFi
MEKi-a
SHP2i
FRS2i
+ FGFR4 inhibitor

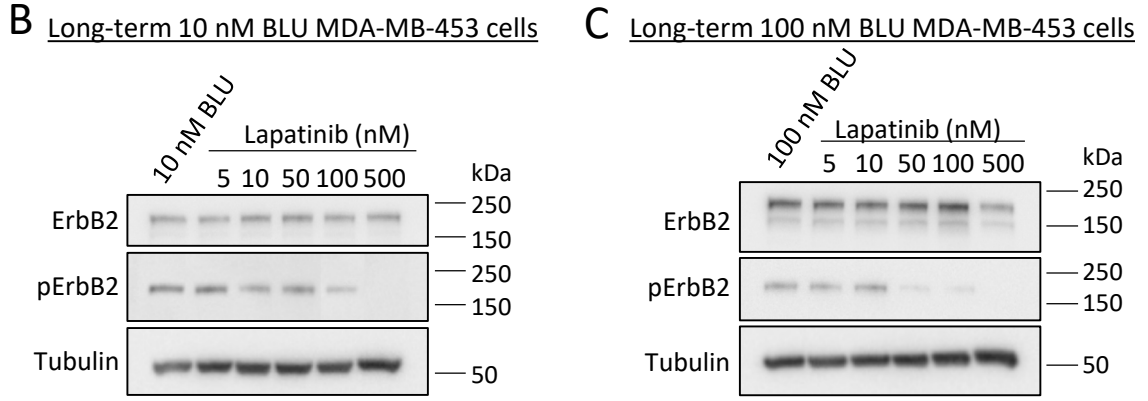
B
Long-term 10 nM BLU MDA-MB-453 cells
10 nM BLU
Lapatinib (nM)
5 10 50 100 500
kDa
ErbB2
pErbB2
Tubulin
250
150
250
150
50
C
Long-term 100 nM BLU MDA-MB-453 cells
100 nM BLU
Lapatinib (nM)
5 10 50 100 500
kDa
ErbB2
pErbB2
Tubulin
250
150
250
150
50

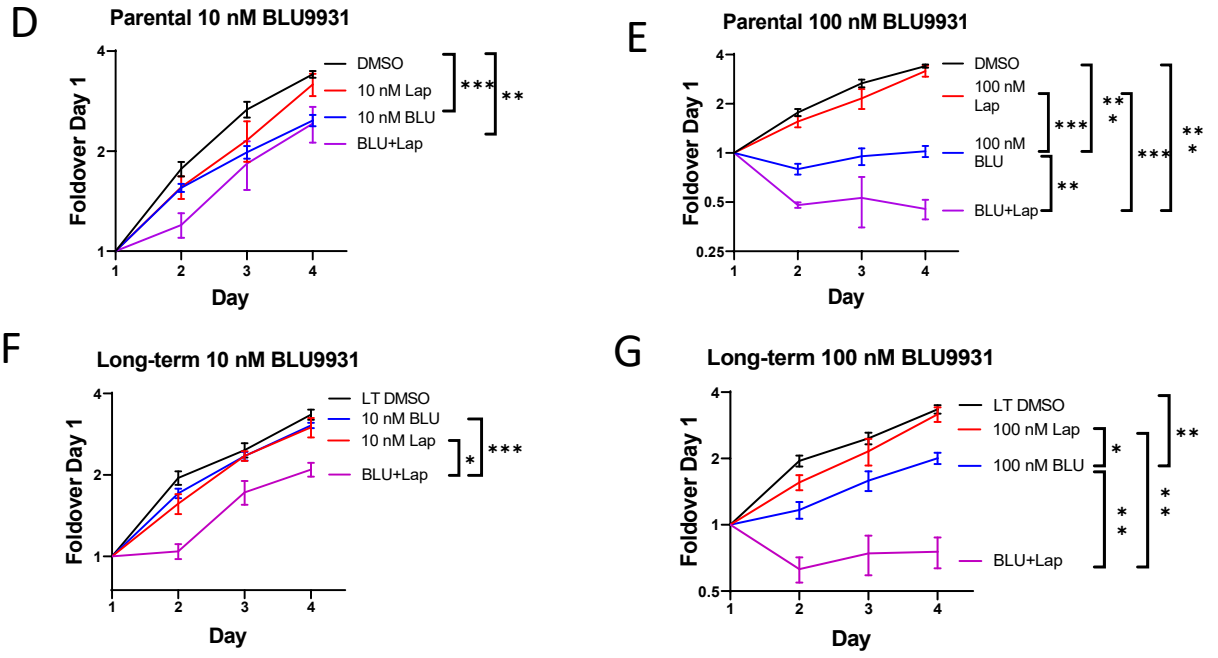
D
Parental 10 nM BLU9931
Foldover Day 1
Day
DMSO
10 nM Lap
10 nM BLU
BLU+Lap
E
Parental 100 nM BLU9931
Foldover Day 1
Day
DMSO
100 nM Lap
100 nM BLU
BLU+Lap
F
Long-term 10 nM BLU9931
Foldover Day 1
Day
LT DMSO
10 nM BLU
10 nM Lap
BLU+Lap
G
Long-term 100 nM BLU9931
Foldover Day 1
Day
LT DMSO
100 nM Lap
100 nM BLU
BLU+Lap

Figure 6

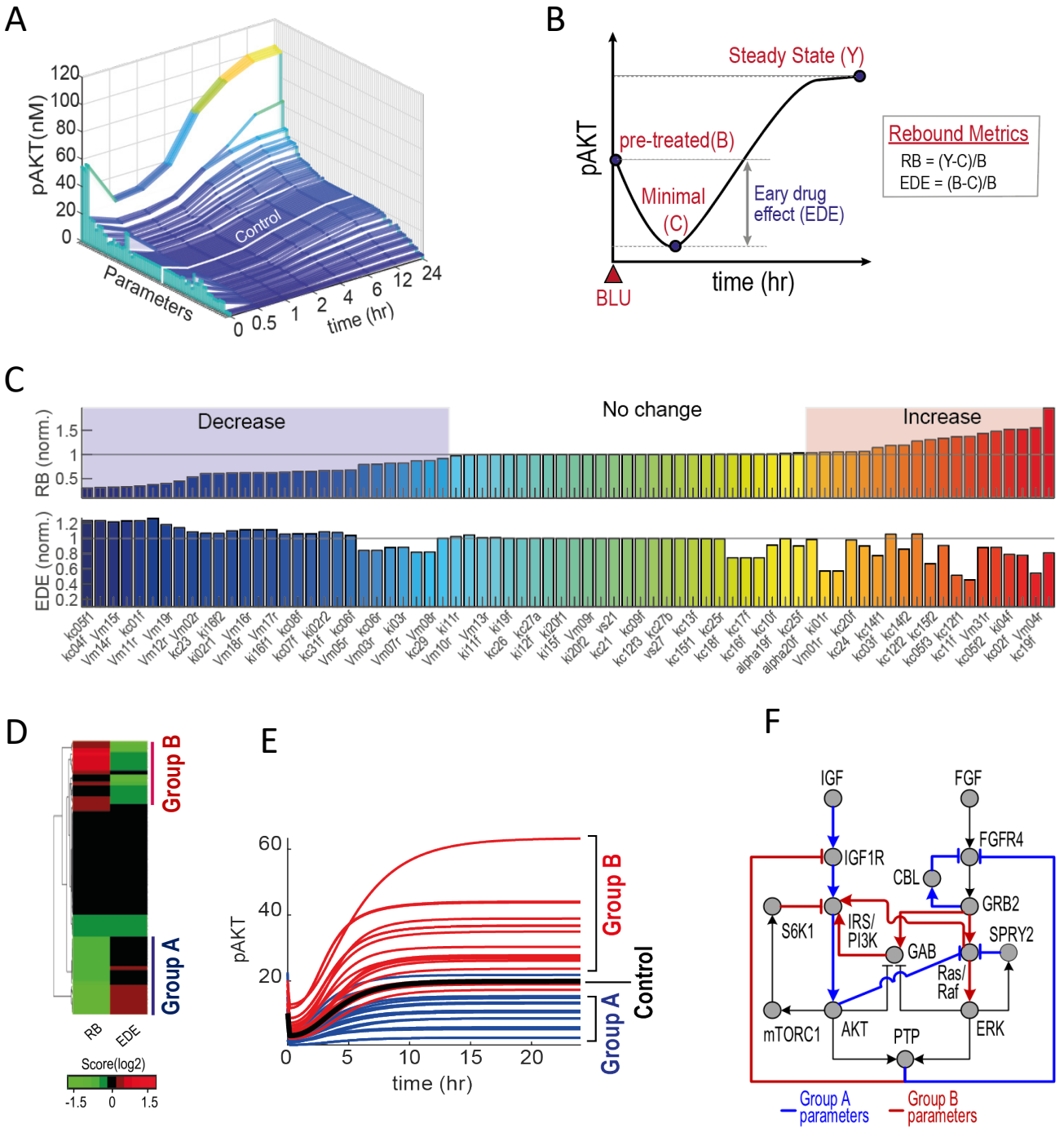
A
pAKT(nM)
120
100
80
60
40
20
0
Control
Parameters
0 0.5 1 2 4 6 12 24
time (hr)
B
Steady State (Y)
pre-treated(B)
Minimal
(C)
Eary drug
effect (EDE)
pAKT
time (hr)
BLU
Rebound Metrics
RB = (Y-C)/B
EDE = (B-C)/B
C
Decrease
No change
Increase
RB (norm.)
1.5
1
0.5
EDE (norm.)
1.2
1
0.8
0.6
0.4
0.2
D
Group B
Group A
RB
EDE
Score(log2)
-1.5 0 1.5
E
60
40
20
pAKT
0 5 10 15 20
time (hr)
Group B
Control
Group A
F
IGF
FGF
IGF1R
FGFR4
CBL
GRB2
S6K1
IRS/
PI3K
GAB
SPRY2
Ras/
Raf
mTORC1
AKT
PTP
ERK
Group A
parameters
Group B
parameters

Figure 7

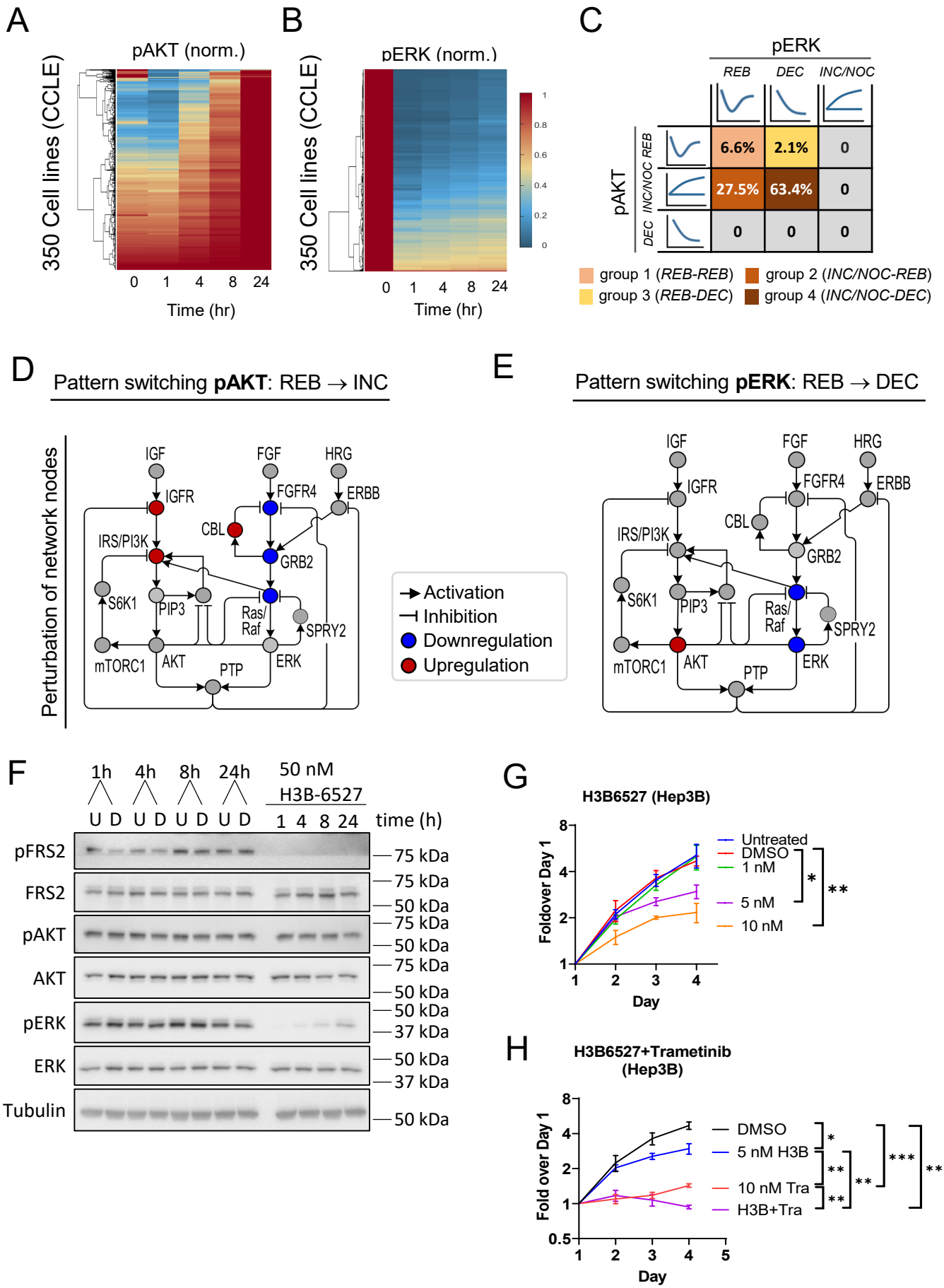
A
pAKT (norm.)
350 Cell lines (CCLE)
0 1 4 8 24
Time (hr)
B
pERK (norm.)
350 Cell lines (CCLE)
0 1 4 8 24
Time (hr)
1
0.8
0.6
0.4
0.2
0
C
pERK
REB
DEC
INC/NOC
pAKT
REB
INC/NOC
DEC
6.6%
2.1%
0
27.5%
63.4%
0
0
0
0
group 1 (REB-REB)
group 2 (INC/NOC-REB)
group 3 (REB-DEC)
group 4 (INC/NOC-DEC)
D
Pattern switching pAKT: REB → INC
Perturbation of network nodes
IGF
FGF
HRG
IGFR
FGFR4
ERBB
CBL
IRS/PI3K
GRB2
S6K1
PIP3
Ras/
Raf
SPRY2
mTORC1
AKT
PTP
ERK
Activation
Inhibition
Downregulation
Upregulation
E
Pattern switching pERK: REB → DEC
IGF
FGF
HRG
IGFR
FGFR4
ERBB
CBL
IRS/PI3K
GRB2
S6K1
PIP3
Ras/
Raf
SPRY2
mTORC1
AKT
PTP
ERK
F
1h
4h
8h
24h
50 nM
H3B-6527
U D U D U D U D
1 4 8 24
time (h)
pFRS2
FRS2
pAKT
AKT
pERK
ERK
Tubulin
75 kDa
75 kDa
50 kDa
75 kDa
50 kDa
75 kDa
50 kDa
50 kDa
37 kDa
50 kDa
37 kDa
50 kDa
G
H3B6527 (Hep3B)
Foldover Day 1
Day
Untreated
DMSO
1 nM
5 nM
10 nM
*
**
H
H3B6527+Trametinib
(Hep3B)
Fold over Day 1
Day
DMSO
5 nM H3B
10 nM Tra
H3B+Tra
*
**
**
**
***
***